

CONSTRAINTS FROM CMB LENSING TOMOGRAPHY WITH PROJECTED BISPECTRA

LEA HARSCOUE^{1,*}, DAVID ALONSO¹, ANDRINA NICOLA^{2,3}, AND ANŽE SLOSAR⁴

¹Department of Physics, University of Oxford, Denys Wilkinson Building, Keble Road, Oxford OX1 3RH, United Kingdom

²Jodrell Bank Centre for Astrophysics, Department of Physics and Astronomy, The University of Manchester, Manchester M13 9PL, UK

³Argelander Institut für Astronomie, Universität Bonn, Auf dem Hügel 71, 53121 Bonn, Germany and

⁴Brookhaven National Laboratory, Physics Department, Upton, NY 11973, USA

Version January 14, 2026

Abstract

We measure the angular power spectrum and bispectrum of the projected overdensity of photometric DESI luminous red galaxies, and its cross-correlation with maps of the Cosmic Microwave Background lensing convergence κ from *Planck*. This analysis is enabled by the use of the “filtered-squared bispectrum” approach, introduced in previous work, which we generalise here to the case of cross-correlations between multiple fields. The projected galaxy bispectrum is detected at very high significance (above 30σ in all redshift bins), and the galaxy-galaxy-convergence bispectrum is detected above 5σ in the three highest-redshift bins. We find that the bispectrum is reasonably well described over a broad range of scales by a tree-level prediction using the linear galaxy bias measured from the power spectrum. We carry out the first cosmological analysis combining projected power spectra (gg and $g\kappa$) and bispectra (ggg only) under a relatively simple model, and show that the galaxy bispectrum can be used in combination with the power spectrum to place a constraint on the amplitude of matter fluctuations, σ_8 , and on the non-relativistic matter fraction Ω_m . We find that data combinations involving the galaxy bispectrum recover constraints on these parameters that are in good agreement with those found from the traditional “ 2×2 -point” combination of galaxy-galaxy and galaxy-convergence power spectra, across all redshift bins.

1. INTRODUCTION

The analysis of projected probes of the large-scale structure (i.e. proxies of the matter fluctuations integrated along the line of sight and mapped onto the celestial sphere) has been one of the most productive areas of cosmology over the last decade. This is thanks to the wide variety of complementary probes we now have access to, and to the fast growth in the cosmic volume we can cover with them. Examples of these probes are the projected clustering of galaxies (Nicola et al. 2020; Vakili et al. 2023; Xu et al. 2023), the gravitational lensing of the Cosmic Microwave Background (CMB lensing) (Lewis & Challinor 2006), galaxy weak lensing (Bartelmann & Schneider 2001; Mandelbaum 2018), or the Sunyaev-Zel’dovich effect (Carlstrom et al. 2002). The combination of galaxy clustering and CMB lensing has been particularly fruitful: by measuring the cross-power spectrum between maps of the CMB lensing convergence κ and the overdensity of galaxies δ_g at different redshifts, and combining it with the auto-correlation of these galaxies, we can simultaneously determine the galaxy bias relation and measure the amplitude of matter fluctuations at the redshifts of these galaxies. This technique, often called “lensing tomography” or “ 2×2 -point analysis”¹, has now been used to place constraints on the growth history with percent-level precision spanning the last 12 billion years ($z \lesssim 3$) (Krolewski et al. 2021; White et al. 2022; Alonso et al. 2023; Farren et al.

2024; Sailer et al. 2025b; Qu et al. 2025; Sailer et al. 2025a; de Belsunce et al. 2025). Including the CMB lensing auto-correlation², one can then extend the growth reconstruction to redshifts above that probed by the highest-redshift galaxy sample used (Farren et al. 2025).

In spite of this success, further information may still be gained from the joint analysis of galaxies and CMB lensing. As the Universe evolves, the matter overdensities grow via non-linear gravitational collapse, which generates non-Gaussian features in their spatial distribution. In this regime, the two-point correlators used in the standard 2×2 -point analysis fail to capture all of the information present in both δ_g and κ . To recover this information, various techniques have been proposed in the literature. On the one hand, field-level analyses constitute the manifestly-optimal approach to extract this information, although they are difficult to deploy in practice, due to their computational complexity, and the need to simulate intricate astrophysical and observational effects present in the data (Jasche & Wandelt 2013; Lavaux et al. 2019; Porqueres et al. 2022, 2023). The alternative approach is to employ well-educated summary statistics, commonly designed by performing non-linear (and sometimes non-local) operation on the data before compressing it onto a small set of measurements (e.g. some form of correlator) (Obreschkow et al. 2013; Friedrich et al. 2018; Eickenberg et al. 2022; Masara et al. 2023; Grewal et al. 2022; Oliveira Franco et al. 2022; Régalo-Saint Blancard et al. 2024; Yip et al. 2024; Cowell

*lea.harscouet@physics.ox.ac.uk

¹ This nomenclature is imprecise and may lead to confusion. We only reluctantly subscribe to it due to its now prevalent use by the community. For clarity, in this work, when discussing “ 2×2 -point” analyses, we will refer to the combination of the galaxy-galaxy and the galaxy-convergence power spectra, and not any other pair of cross-correlations.

² Often referred to as “ 3×2 -point”, not to be confused with the same technique when applied to galaxy weak lensing – even though often more than 3 correlations in total are actually used in both cases.

et al. 2024). Within this category, the bispectrum (i.e. the Fourier- or harmonic-space third-order correlator) stands out for several reasons. First, the bispectrum is the lowest-order non-Gaussian summary statistic, and thus should contain significantly more information than other correlators for mildly non-Gaussian fields. Secondly, it is a theoretically tractable observable, in the sense that predictions for it can be made from first principles (e.g. via perturbation theory), without the need for simulations that must encompass all physical effects present in the data (Scoccimarro et al. 1999; Bernardeau et al. 2002; Simpson et al. 2011; Montandon et al. 2023).

Incorporating the bispectrum in cosmological analyses can be a significant challenge, however, in comparison with the standard power-spectrum-based studies. First, optimal bispectrum estimators are often significantly more computationally challenging than their power spectrum versions (Scoccimarro 2015; Philcox 2021; Philcox & Flöss 2024). Furthermore, unlike the fairly compact power spectrum, information in the bispectrum measurement is spread over a large number of “triangle configurations”. Thirdly, it is often difficult to derive robust estimates of the bispectrum uncertainties, and its covariance with the power spectrum (Biagetti et al. 2022). Simulations may be used in this case, but a large number of them is needed to ensure convergence over the large number of triangle configurations available. Similarly, the mode-coupling matrix – which accounts for mode loss and coupling induced by the survey geometry – is also numerically challenging to evaluate due to the sheer number of pairwise combinations of triangle configurations (although the survey window function has been studied for specific bispectrum statistics in e.g. Sugiyama et al. 2019). Finally, bispectrum predictions may be slow to produce from first principles, mostly due again to the large number of configurations. Partly because of these difficulties, the projected bispectrum has not been widely exploited in cosmological large-scale structure analyses. Although the bispectrum has been considered in the context of weak lensing (Cooray & Hu 2001; Takada & Jain 2004; Munshi et al. 2020a), most existing constraints are based on specific real-space two-point correlations (Gatti et al. 2022; Secco et al. 2022; Porth et al. 2024; Burger et al. 2024). One of the few examples present in the literature is the recent measurements of the projected galaxy-galaxy- κ bispectrum presented in Farren et al. (2023).

Recently, Harscouet et al. (2025) (H25 hereafter) introduced the filtered-squared bispectrum estimator (FSB), addressing some of the difficulties mentioned above, and significantly simplifying the analysis of projected bispectra. The FSB is similar in spirit to the skew-spectrum (Cooray 2001; Calabrese et al. 2010; Smidt et al. 2010; Moradinezhad Dizgah et al. 2020; Munshi et al. 2020b) (i.e. the cross-correlation between a given field and its square), introducing a filtering operation that allows it to recover different bispectrum configurations. Most importantly, by employing power spectrum techniques, H25 demonstrated that the FSB covariance (including its covariance with the power spectrum) may be accurately estimated using fast analytical methods in a completely data-driven manner, solving one of the main hurdles of bispectrum analysis. In this paper, we exploit the FSB to measure the galaxy-galaxy-galaxy and galaxy-galaxy- κ bispectrum in real data, in combination with the standard 2×2 -point data vector. We will use these measurements to carry out a first tentative cosmological analysis combining projected power spectra and bispectra, quantifying the ability of the bispectrum to reduce the final parameter uncertainties, and to test the robustness of cosmological constraints, through the consistency between

different data combinations.

The paper is structured as follows. Section 2 presents the FSB estimator, and the extension we introduce here to the case of multi-field cross-correlations. It also describes the model we will use to interpret our measurements, and our parameter inference pipeline. The galaxy samples and CMB lensing data we use in the analysis are described in Section 3. Our results, including an assessment of the ggg and $gg\kappa$ bispectrum detections, the complementarity of different data combinations, and the cosmological constraints derived from the gg , $g\kappa$ and ggg measurements, are presented in Section 4. Finally, Section 5 summarises our results and discusses potential avenues for future exploration.

2. METHODS

2.1. FSB review

In this section we provide a short summary of the Filtered-Squared Bispectrum (FSB), first introduced in H25 – for a more complete introduction, please refer to section 2.2 of that paper.

2.1.1. The estimator

Let us consider a scalar field $a(\hat{\mathbf{n}})$ defined on the sphere, and a filter W_ℓ^L which only has significant support over a compact range of angular scales $\ell \in L$. Note that this choice of filter is not unique, and that we can perform the following steps for a set of filters defined over different multipole ranges – but for the sake of simplicity we focus for now on one filter W_ℓ^L . Now let us construct a “filtered-squared” version of a , by first filtering it in harmonic space so as to only keep the information coming from the scales selected by the W_ℓ^L filter:

$$a_L(\hat{\mathbf{n}}) \equiv \mathcal{S}^{-1} [W_\ell^L \mathcal{S}[a]_{\ell m}]_{\hat{\mathbf{n}}}, \quad (1)$$

where we use $\mathcal{S}, \mathcal{S}^{-1}$ as shorthands for the spherical harmonic transform and its inverse respectively. We then square the filtered field in real space: $a_L^2(\hat{\mathbf{n}}) \equiv (a_L(\hat{\mathbf{n}}))^2$.

The FSB is the angular power spectrum of $(a_L^2)(\hat{\mathbf{n}})$ with the original field $a(\hat{\mathbf{n}})$: in the simplest case (that of full-sky observations, with the power spectrum estimated at each integer ℓ), this is simply

$$\hat{\Phi}_{LL\ell}^{aaa} \equiv \frac{1}{2\ell + 1} \sum_m (a_L^2)_{\ell m} a_{\ell m}^*. \quad (2)$$

In the presence of a mask $w_a(\hat{\mathbf{n}})$ associated with field $a(\hat{\mathbf{n}})$, and using bandpowers (i.e. bins of ℓ) labelled by an index b , we replace this by the pseudo- C_ℓ (PCL) estimator, as implemented in the NaMaster code³ (Alonso et al. 2019). This version of the FSB estimator accounts for mode-coupling effects introduced when taking the power spectrum of two fields partially defined on the sky. However, the back and forth between real and harmonic space during the early filtering step inevitably introduces some additional mode coupling which is not fully accounted for in the estimator; H25 verified that the estimator remained robust to those residual mode coupling effects, by measuring the (largely negligible) effect caused by masks of varied complexity on the FSB estimator.

³ <https://github.com/LSSTDESC/NaMaster>

2.1.2. Relation to the projected bispectrum

We can relate the FSB estimator to the full projected bispectrum of field a , $b_{\ell_1 \ell_2 \ell_3}^{aaa}$, by expanding $(a_L^2)_{\ell m}$ in Eq. 2 in terms of the harmonic coefficients of field a . This allows us to write

$$\hat{\Phi}_{LL\ell}^{aaa} = \sum_{(\ell m)_{123}} \mathcal{G}_{\ell_1 \ell_2 \ell_3}^{m_1 m_2 m_3} K_{\ell_1 \ell_2 \ell_3}^{LL\ell} a_{\ell_1 m_1} a_{\ell_2 m_2} a_{\ell_3 m_3}, \quad (3)$$

where the Gaunt coefficient \mathcal{G} ensures that only closed triangle configurations of (ℓ_1, ℓ_2, ℓ_3) contribute to the estimator, and where we have defined the FSB kernel:

$$K_{\ell_1 \ell_2 \ell_3}^{L_1 L_2 \ell} \equiv \frac{W_{\ell_1}^{L_1} W_{\ell_2}^{L_2} W_{\ell_3}^{\ell}}{2\ell_3 + 1}, \quad (4)$$

which ensures that the triangles in question are those that have two sides with scales $\ell_1 \sim \ell_2 \in L$, and one with scale $\ell_3 = \ell$. In the more common case of using bandpowers, $\ell_3 \in b$, the denominator is replaced by the total number of modes in the bandpower, $N_b \equiv \sum_{\ell_3 \in b} (2\ell_3 + 1)$.

Upon taking the expectation value of Eq. 3, we recover an expression for the FSB which depends on the projected bispectrum $b_{\ell_1 \ell_2 \ell_3}^{aaa}$:

$$\Phi_{LL\ell}^{aaa} = \sum_{(\ell)_{123}} h_{\ell_1 \ell_2 \ell_3}^2 K_{\ell_1 \ell_2 \ell_3}^{LL\ell} b_{\ell_1 \ell_2 \ell_3}^{aaa}, \quad (5)$$

where

$$h_{\ell_1 \ell_2 \ell_3}^2 \equiv \frac{(2\ell_1 + 1)(2\ell_2 + 1)(2\ell_3 + 1)}{4\pi} \begin{pmatrix} \ell_1 & \ell_2 & \ell_3 \\ 0 & 0 & 0 \end{pmatrix}^2, \quad (6)$$

with the squared term a $3j$ Wigner symbol.

The FSB $\Phi_{LL\ell}^{aaa}$ is therefore an efficient estimator for the projected bispectrum $b_{\ell_1 \ell_2 \ell_3}^{aaa}$: it is fast to compute, and robust to mode-coupling effects caused by incomplete sky observations. It is also a convenient higher-order statistics for which analytical predictions can be constructed from first principles (as we will see in Section 2.4.3).

2.1.3. FSB covariance

Another appealing feature of the FSB is the fact that its covariance matrix can be estimated easily, accurately, and in a model-independent way, using analytical methods. This is possible by reusing various techniques developed in the context of power spectrum covariance estimation. In H25, the FSB covariance estimate is built following these steps:

1. Pushing the FSB reinterpretation of the bispectrum as a power spectrum between a and a_L^2 , we can use existing techniques (García-García et al. 2019) to obtain a first analytical approximation of the covariance, by assuming that both a and a_L^2 are Gaussian fields. Although this assumption is in general incorrect, since a_L^2 cannot be Gaussian even if a is (which it generally is not), H25 shows it recovers all purely diagonal terms – both disconnected and connected – contributing to the covariance. This is not entirely surprising, as the ‘‘Gaussian’’ power spectrum covariance is known to dominate the statistical uncertainties even for the highly non-Gaussian fields commonly encountered in large-scale structure (Li et al. 2019).

2. We add to this first estimate two leading-order off-diagonal terms which we derived analytically, coined N_{222} (disconnected term which contributes to the FSB auto-covariance) and N_{32} (partially-connected term which contributes to the FSB- C_ℓ cross-covariance).
3. The two latter terms are scaled by the inverse of the effective sky fraction f_{sky} , to account for the impact of mode loss in cut-sky observations.

This covariance estimate is reasonably accurate and can be estimated directly from the data, as it only depends on 2-point and 3-point correlators (i.e. the power spectra and FSBs of the field involved). For completeness we repeat here the expressions for N_{222} and N_{32} derived in H25 (before any f_{sky} scaling):

$$\text{Cov}_{N_{222}} \left(\hat{\Phi}_{LL\ell}^{aaa}, \hat{\Phi}_{L'L'\ell'}^{aaa} \right) = \frac{C_{\ell}^{aa} C_{\ell'}^{aa} W_{\ell}^L W_{\ell'}^{L'}}{\pi} \times \sum_{\ell_1} (2\ell_1 + 1) W_{\ell_1}^L W_{\ell_1}^{L'} C_{\ell_1}^{aa} \begin{pmatrix} \ell & \ell' & \ell_1 \\ 0 & 0 & 0 \end{pmatrix}^2, \quad (7)$$

$$\text{Cov}_{N_{32}} \left(\hat{\Phi}_{LL\ell}^{aaa}, C_{\ell'}^{aa} \right) = \frac{4W_{\ell'}^L C_{\ell'}^{aa} \Phi_{LL\ell}^{aaa}}{(2\ell + 1)}, \quad (8)$$

where $\Phi_{LL\ell}^{aaa}$ is a generalisation of the standard FSB in which one of the filtered copies of the field is restricted to the contributions from a single multipole ℓ .

2.2. Multi-field FSB

One can easily extend the definition of the FSB to more general cases by modifying some of the analysis choices made, without impacting the efficiency and accuracy of the estimator:

- We could use two different fields α and β to build the filtered-squared map, and a third field γ to correlate it with. This straightforward modification would allow us to probe the projected bispectrum of multiple fields $b_{\ell_1 \ell_2 \ell_3}^{\alpha\beta\gamma}$, with obvious applications in the context of cross-correlations.
- We could probe arbitrary triangle configurations beyond the close-to-isosceles ones the FSB is sensitive to. This can be done by replacing the ‘‘squaring’’ step by a multiplication of the field filtered on two different scales. The resulting estimator would be directly sensitive to configurations of the form $b_{L_1 L_2 \ell}$, where L_1 and L_2 are the two filters being multiplied, and ℓ is the multipole at which the power spectrum is calculated.

One advantage of the FSB with its unique filter definition is that it keeps the dimensionality of the resulting data vector to a reasonable minimum, only selecting triangle configurations of interest (e.g. the squeezed limit of the bispectrum, via the selection of triangles close to isosceles). The main difficulty in the case of the multi-filter estimator is the significantly larger size of the resulting data vector. Unless significant information is encoded in the triangle configurations neglected by the vanilla FSB estimator, this could spoil the efficiency of the estimator for only modest gains in terms of final parameter constraints. We therefore leave the exploration of the multi-filter estimator for future work.

Instead, in this paper we focus on the multi-field version of the estimator. In particular, we will consider cross-correlating a filtered-squared field $a_L^2(\hat{\mathbf{n}})$ with another field $f(\hat{\mathbf{n}})$, effectively probing their cross-bispectrum $b_{\ell_1\ell_2\ell_3}^{aaf}$. This is the simplest option to generalize the FSB estimator to cross correlations: another option would be to correlate $(af)_L$ with a , but this comes with a few drawbacks. Among these are the fact that real-space multiplication of a and f might discard some information coming from regions of f that do not overlap with a ; and that $(af)_L \times a$ exhibits less symmetry than $(a^2)_L \times f$, which would result in a more complicated analytical covariance matrix.

This measurement requires very few changes to the estimator: our original expression for the single-field FSB (Eq. 2) becomes

$$\hat{\Phi}_{LL\ell}^{aaf} \equiv \frac{1}{2\ell+1} \sum_m (a_L^2)_{\ell m} f_{\ell m}^* \quad (9)$$

or the corresponding pseudo- C_ℓ estimator in the case of cut-sky observations.

This slight change in the estimator carries over to the covariance: although the analytical Gaussian covariance and N_{222} terms are easily generalised to this multi-field case, the N_{32} term changes more significantly. The multi-field expressions for N_{222} and N_{32} are derived in Appendix C, where we also derive expressions for cross-covariance terms between single-field and multi-field FSBs, as well as the associated C_ℓ s. For completeness, the most relevant N_{222} and N_{32} terms read:

$$\text{Cov}_{N_{222}} \left(\hat{\Phi}_{LL\ell}^{aaf}, \hat{\Phi}_{L'L'\ell'}^{aaf} \right) = \frac{W_{\ell'}^L W_{\ell'}^{L'} C_{\ell'}^{af} C_{\ell'}^{af}}{\pi} \times \sum_{\ell_1} (2\ell_1 + 1) \begin{pmatrix} \ell & \ell_1 & \ell' \\ 0 & 0 & 0 \end{pmatrix}^2 W_{\ell_1}^L W_{\ell_1}^{L'} C_{\ell_1}^{aa}, \quad (10)$$

$$\text{Cov}_{N_{32}} \left(\hat{\Phi}_{LL\ell}^{aaf}, C_{\ell'}^{af} \right) = \frac{2 W_{\ell'}^L}{(2\ell' + 1)} \times \left(C_{\ell'}^{aa} \Phi_{L'\ell'}^{aff} + C_{\ell'}^{af} \Phi_{L'\ell'}^{aaf} \right). \quad (11)$$

Note that the N_{32} term is split into two contributions (compared to the single term in Eq. 8), since some of the symmetries present in the single-field FSB are broken after introducing a different field. This will increase the computational time for this term twofold, which is easily manageable.

Note that each of the fields involved have, in general, different masks. The resulting mode-coupling will differ from the single-field/single-mask case, but the effect is entirely accounted for by the PCL estimator, which automatically handles the multi-field case for power spectra. Some consideration must be put into the scaling of the N_{222} and N_{32} covariance terms with the effective sky fraction. For instance, if one were to compute the covariance of $\hat{\Phi}_{LL\ell}^{aaa}$ with $\hat{\Phi}_{L'L'\ell'}^{aaf}$, would they scale these additional terms using $f_{\text{sky}} \equiv \langle w_a w_a \rangle$ (the natural choice for the single-field FSB), or $f_{\text{sky}} \equiv \langle w_a w_f \rangle$ (the relevant one for the multi-field case)? Counter-intuitively, the correct approach in this specific example is to use $f_{\text{sky}} \equiv \langle w_a w_a \rangle$, with no mention of w_f . We derive these results in Appendix C.3, and empirically confirm the accuracy of these scalings using simulations.

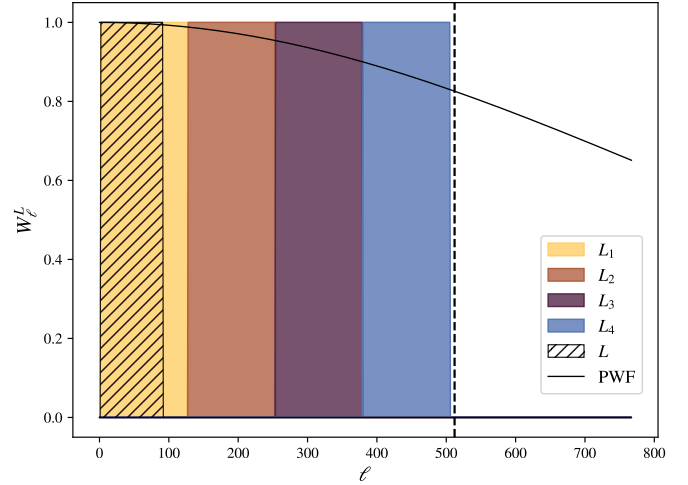


Figure 1. Filters used in this analysis. The colourful set represents the 4 filters used in Section 4.1 to detect the FSB on a wide range of scales; the hatched filter is the single filter used for deriving cosmological constraints in Section 4.2. The latter remains below the conservative ℓ_{max}^B cut in all redshift bins, and the former are defined below the $2N_{\text{side}}$ threshold, beyond spherical harmonic transforms may become unreliable. We also show the pixel window function (solid black line) corresponding to the map resolution.

2.3. Maps and power spectrum measurements

When analysing the data described in Section 3, we will construct maps of the galaxy overdensity and CMB convergence fields using the HEALPix pixelisation scheme (Górski et al. 2005), with a resolution parameter $N_{\text{side}} = 256$, corresponding to a pixel size of $\delta\theta \sim 0.23^\circ$.

We will measure the power spectra and FSBs of these maps as described in the previous sections. In particular, we will measure the galaxy-galaxy and galaxy-convergence power spectra (C_ℓ^{gg} and C_ℓ^{gk}), as well as the “galaxy³” and “galaxy²×convergence” FSBs ($\Phi_{LL\ell}^{ggg}$ and $\Phi_{LL\ell}^{ggk}$). We will make measurements of the FSBs using two different sets of filters, shown in Fig. 1:

- To determine the detectability of the projected bispectrum, we will measure the FSB in four filters below the $2N_{\text{side}}$ threshold. These four consecutive top-hat filters each have width $\Delta\ell = 126$, partitioning the multipole range $\ell \in [2, 506]$.
- To perform a first cosmological analysis of the FSB, we will measure it on a single filter, covering the range $\ell \in [2, 92]$. This is to ensure that the bispectrum measurements used in the analysis only include information from angular scales where our tree-level model (see Section 2.4) is reliable.

The power spectra and FSBs are measured over the full range $\ell < 3N_{\text{side}}$, although we discard all data above $\ell \geq 2N_{\text{side}}$, where the HEALPix spherical harmonic transform can be unreliable. We will also discard all FSB measurements that break the triangle inequality, where the bispectrum signal vanishes. The spectra we compute in Section 4.1 were measured in 24 bandpowers with equal width, $\Delta\ell = 21$, covering the range $\ell < 2N_{\text{side}} = 512$.

Finally, we must also account for the impact of pixelisation on our measurements. The most important effect is the loss of power on scales comparable to that of the pixel size when the map in question is effectively the average of its infinite-resolution version over the pixel area. This loss of power can be

captured in terms of the pixel window function (PWF) ℓ_ℓ . In practice, only the galaxy overdensity maps used in this analysis are affected by the PWF, as the lensing convergence data is provided natively in the form of its harmonic coefficients, which we then sample at the pixel positions when transforming them into a map. Instead of correcting our measurements for the PWF, we include them in our theoretical model. This can be done by simply modifying the filters entering the FSB kernel (Eq. 4) as e.g.:

$$W_\ell^L \rightarrow \ell_\ell W_\ell^L. \quad (12)$$

This must be done for the filters and bandpower window functions corresponding to any field affected by the PWF (i.e. the galaxy overdensity, but not κ in our case). Power spectra should be likewise corrected by the PWF where relevant. Note that any pure shot noise contribution (namely the power spectrum shot noise, N_ℓ^{gg} , and the ggg FSB noise term in Eq. 31) should not be corrected for the PWF, as white noise spectra remain constant regardless of the pixelization scheme⁴.

2.4. Theory and modelling

This section presents the theoretical framework we will use to make predictions for the power spectrum and FSB measurements we present in Section 4, as a function of cosmological and galaxy bias parameters.

2.4.1. Galaxy clustering and CMB lensing

We will study the power spectrum and bispectrum of two large-scale structure tracers projected on the celestial sphere: the CMB lensing convergence κ , and the angular galaxy overdensity δ_g^{2D} . These tracers can be connected with the three-dimensional matter and galaxy overdensities (δ_m, δ_g) via line-of-sight integrals of the form

$$\delta_g^{2D}(\hat{\mathbf{n}}) = \int d\chi q_g(\chi) \delta_g(\chi \hat{\mathbf{n}}, z(\chi)), \quad (13)$$

$$\kappa(\hat{\mathbf{n}}) = \int d\chi q_\kappa(\chi) \delta_m(\chi \hat{\mathbf{n}}, z(\chi)). \quad (14)$$

Here, $\hat{\mathbf{n}}$ is a unit vector pointing along the line of sight, χ is the radial comoving distance, and the radial kernels for κ and δ_g^{2D} are

$$q_g(\chi) = H(z) p(z), \quad (15)$$

$$q_\kappa(\chi) = \frac{3}{2} \Omega_m H_0^2 \chi (1+z) \frac{\chi_{\text{CMB}} - \chi}{\chi_{\text{CMB}}}, \quad (16)$$

where $H(z)$ is the expansion rate at redshift z (implicitly corresponding to comoving distance χ in the lightcone) and H_0 is the expansion rate today. χ_{CMB} is the comoving distance to the last-scattering surface, Ω_m is the fraction of non-relativistic matter, and $p(z)$ is the redshift distribution of the galaxy sample under study.

We will use a perturbative expansion in Eulerian space, up to second order, to connect the galaxy and matter overdensities (Fry & Gaztanaga 1993; McDonald & Roy 2009). Specifically,

⁴ This can be understood in terms of a purely Poisson process, in which the measurements on different pixels remain statistically independent regardless of the pixel size.

in Fourier space this reads

$$(\delta_m)_{\mathbf{k}} = \delta_{\mathbf{k}}^{(1)} + \delta_{\mathbf{k}}^{(2)} \quad (17)$$

$$(\delta_g)_{\mathbf{k}} = b_1 \left[\delta_{\mathbf{k}}^{(1)} + \delta_{\mathbf{k}}^{(2)} \right] + \frac{b_2}{2} ((\delta^{(1)})^2)_{\mathbf{k}} + b_s (s^2)_{\mathbf{k}}, \quad (18)$$

where $\delta_{\mathbf{k}}^{(1)}$ is the linear-order matter overdensity, which we assume to be Gaussian, $\delta_{\mathbf{k}}^{(2)}$ is the contribution to the matter overdensity at second order in standard perturbation theory, and $s^2 \equiv s_{ij} s^{ij}$ is the square of the traceless shear field, with

$$s_{ij,\mathbf{k}} \equiv \left(\frac{k_i k_j}{k^2} - \frac{1}{3} \right) \delta_{\mathbf{k}}^{(1)}. \quad (19)$$

The quantities b_1 , b_2 , and b_s are the linear, quadratic, and tidal bias parameters. The different terms in Eq. 17 can be written in terms of the linear overdensity as

$$\delta_{\mathbf{k}}^{(2)} = \int D\mathbf{k}_1 D\mathbf{k}_2 F_2(\mathbf{k}_1, \mathbf{k}_2) \delta_{\mathbf{k}_1}^{(1)} \delta_{\mathbf{k}_2}^{(1)}, \quad (20)$$

$$((\delta^{(1)})^2)_{\mathbf{k}} = \int D\mathbf{k}_1 D\mathbf{k}_2 Q_2(\mathbf{k}_1, \mathbf{k}_2) \delta_{\mathbf{k}_1}^{(1)} \delta_{\mathbf{k}_2}^{(1)}, \quad (21)$$

$$(s^2)_{\mathbf{k}} = \int D\mathbf{k}_1 D\mathbf{k}_2 T_2(\mathbf{k}_1, \mathbf{k}_2) \delta_{\mathbf{k}_1}^{(1)} \delta_{\mathbf{k}_2}^{(1)}, \quad (22)$$

where we use the shorthand notation

$$\int D\mathbf{k}_1 D\mathbf{k}_2 \equiv \int \frac{d^3 k_1}{(2\pi)^3} \frac{d^3 k_2}{(2\pi)^3} (2\pi)^3 \delta^D(\mathbf{k} - \mathbf{k}_1 - \mathbf{k}_2),$$

and we have defined the perturbation theory kernel F_2 , the quadratic kernel Q_2 , and the tidal kernel T_2 as:

$$F_2(\mathbf{k}_1, \mathbf{k}_2) = \frac{5}{7} + \frac{1}{2} \mu_{12} \left(\frac{k_1}{k_2} + \frac{k_2}{k_1} \right) + \frac{2}{7} \mu_{12}^2, \quad (23)$$

$$Q_2(\mathbf{k}_1, \mathbf{k}_2) = 1, \quad (24)$$

$$T_2(\mathbf{k}_1, \mathbf{k}_2) = \mu_{12}^2 - \frac{1}{3}, \quad (25)$$

with $\mu_{12} \equiv (\mathbf{k}_1 \cdot \mathbf{k}_2) / (|\mathbf{k}_1| |\mathbf{k}_2|)$.

2.4.2. Power spectrum modelling

In a flat universe, the angular power spectrum $C_\ell^{\alpha\beta}$ of two projected quantities α and β is related to the power spectrum of the associated 3D fields, $P^{\alpha\beta}(k, z)$ via

$$C_\ell^{\alpha\beta} = \int \frac{d\chi}{\chi^2} q_\alpha(\chi) q_\beta(\chi) P^{\alpha\beta}(k_\ell(\chi), z(\chi)), \quad (26)$$

where $k_\ell(\chi) \equiv (\ell + 1/2)/\chi$ is the 3D wavenumber associated with the angular scale ℓ , and $q_\alpha(\chi)$ is the radial kernel of the α field. This relation is accurate in the Limber approximation (Limber 1953; LoVerde & Afshordi 2008), which holds for the wide radial kernels used in this work.

Since we will study the galaxy auto-correlation and its cross-correlation with the lensing convergence, we must develop a model for the 3D galaxy-galaxy and galaxy-matter power spectra, $P^{gg}(k, z)$ and $P^{gm}(k, z)$. For simplicity, we will restrict our analysis to large scales, where both spectra are well described at tree level. Using the perturbative bias expansion described in the previous section, the only tree-level contribution is due to the linear galaxy bias term, given by

$$P^{gg}(k, z) = b_1^2 P^{mm}(k, z), \quad P^{gm}(k, z) = b_1 P^{mm}(k, z), \quad (27)$$

where $P^{mmm}(k, z)$ is the matter power spectrum. We also account for Redshift-Space Distortions (RSDs) in our modelling of the power spectra by adding a RSD term, linear in the matter density field, to the linear bias expansion.

We estimate and subtract the contribution from shot noise to the galaxy-galaxy power spectrum as described in [White et al. \(2022\)](#).

2.4.3. Bispectrum Modelling

As in the case of the power spectrum, the projected bispectrum of any three fields $b_{\ell_1 \ell_2 \ell_3}^{\alpha\beta\gamma}$ can be computed from their 3D bispectrum $B^{\alpha\beta\gamma}(k_1, k_2, k_3, z)$ via the Limber approximation:

$$b_{\ell_1 \ell_2 \ell_3}^{\alpha\beta\gamma} = \int d\chi \frac{q^\alpha(\chi) q^\beta(\chi) q^\gamma(\chi)}{\chi^4} \times B^{\alpha\beta\gamma}(k_{\ell_1}(\chi), k_{\ell_2}(\chi), k_{\ell_3}(\chi), z(\chi)), \quad (28)$$

where q^ι is the ι field's radial kernel, and $k_\ell \equiv (\ell + 1/2)/\chi$.

In this work we will focus on the galaxy-galaxy-galaxy and galaxy-galaxy-convergence bispectra (ggg and $gg\kappa$ hereafter), and hence must model the 3D ggg and ggm bispectra. We do not include the convergence-convergence-galaxy ($\kappa\kappa g$) bispectrum in this work, which might require a more complex modelling of the lensing reconstruction noise and is expected to have a lower signal than the ggg and $gg\kappa$ bispectra. As in the case of the power spectrum, we will do this at lowest order in perturbation theory (i.e. tree level). Using the perturbative bias expansion introduced in Section 2.4.1, the corresponding bispectra are given by (see [Schmittfull et al. 2015](#); [Desjacques et al. 2018](#); [Cagliari et al. 2025](#)):

$$B^{ggg}(k, k', k'') = b_1^3 \left(2 F_2(\mathbf{k}, \mathbf{k}') P_k P_{k'} + 2 \text{perms.} \right) + \frac{b_1^2 b_2}{2} \left(2 Q_2(\mathbf{k}, \mathbf{k}') P_k P_{k'} + 2 \text{perms.} \right) + b_1^2 b_s \left(2 T_2(\mathbf{k}, \mathbf{k}') P_k P_{k'} + 2 \text{perms.} \right), \quad (29)$$

$$B^{ggm}(k, k', k'') = b_1^2 \left(2 F_2(\mathbf{k}, \mathbf{k}') P_k P_{k'} + 2 \text{perms.} \right) + \frac{b_1 b_2}{2} \left(2 Q_2(\mathbf{k}, \mathbf{k}'') P_k P_{k''} + 1 \text{perm.} \right) + b_1 b_s \left(2 T_2(\mathbf{k}, \mathbf{k}'') P_k P_{k''} + 1 \text{perm.} \right). \quad (30)$$

P_k denotes the linear matter power spectrum. The cyclical permutations for the ggg bispectrum are, explicitly, $\{\mathbf{k}, \mathbf{k}'\}$, $\{\mathbf{k}', \mathbf{k}''\}$, and $\{\mathbf{k}'', \mathbf{k}\}$. In turn, the permutations in the $gg\kappa$ case are the same for the linear term, but only $\{\mathbf{k}', \mathbf{k}''\}$ and $\{\mathbf{k}'', \mathbf{k}\}$ contribute for the quadratic and tidal terms. Once computed, the 3D bispectrum $B^{ggg}(\mathbf{k}, \mathbf{k}', \mathbf{k}'')$ (B^{ggm}) can be inserted into Eq. 28 to recover the projected bispectrum $b_{\ell\ell'\ell''}^{ggg}$ ($b_{\ell\ell'\ell''}^{ggm}$)⁵.

⁵ Note that we use the notation $b^{gg\kappa}$ (as opposed to b^{ggm}) to highlight the fact that we are using the CMB convergence κ as tracer for the matter on the line of sight, m – this relationship is encoded in the projection kernel $q_\kappa(\chi)$ (Eq. 14).

Due to the stochastic nature of discrete tracers such as galaxies, we must take into account additional contributions to the projected bispectrum due to shot noise. Assuming galaxy tracers can be modelled via Poisson statistics, these terms are given in harmonic space by

$$N_{\ell\ell'\ell''}^{ggg} = \bar{n}^{-2} + \bar{n}^{-1} \left(C_\ell^{gg} + C_{\ell'}^{gg} + C_{\ell''}^{gg} \right) \quad (31)$$

$$N_{\ell\ell'\ell''}^{gg\kappa} = \bar{n}^{-1} C_{\ell''}^{g\kappa} \quad (32)$$

where \bar{n} denotes the angular number density of galaxies per steradian in the survey. The derivation of Eq. 31 can be found in Appendix D of H25; we provide a derivation of Eq. 32 in Appendix B. The final quantity we convert to an FSB using Eq. 5 is the addition of the projected theoretical bispectrum and of these noise terms. It is worth emphasising that, since these stochastic contributions depend on the signal power spectra (C_ℓ^{gg} and $C_\ell^{g\kappa}$), they could potentially help break parameter degeneracies.

2.4.4. Magnification

Our discussion in the preceding sections has failed to include the impact of lensing magnification in the observed galaxy overdensity. Gravitational lensing modifies the observed positions of galaxies, effectively washing out structure around foreground lenses, and modifies the observed flux via magnification, typically bringing fainter galaxies into the selected sample. The competition between these two effects leads to an additive contribution to the observed galaxy overdensity, given by

$$\Delta\delta_g^{2D, \text{mag}}(\hat{\mathbf{n}}) = \int d\chi q_\mu(\chi) \delta_m(\chi \hat{\mathbf{n}}, z(\chi)), \quad (33)$$

and where the magnification lensing kernel is

$$q_\mu(\chi) \equiv \frac{3}{2} \Omega_m H_0^2 (1+z) \chi \int_{z(\chi)}^\infty dz' (5s-2) p(z') \frac{\chi(z') - \chi}{\chi}, \quad (34)$$

where s is the logarithmic slope of the cumulative number count of sources as a function of magnitude at the magnitude limit.

The presence of magnification modifies the galaxy-galaxy and galaxy-convergence power spectra as

$$C_\ell^{gg} = C_\ell^{gg,0} + C_\ell^{g\mu} + C_\ell^{\mu\mu}, \quad (35)$$

$$C_\ell^{g\kappa} = C_\ell^{g\kappa,0} + C_\ell^{\mu\kappa}, \quad (36)$$

where

$$C_\ell^{gg,0} = \int \frac{d\chi}{\chi^2} q_g^2(\chi) P^{gg}(k_\ell, z), \quad (37)$$

$$C_\ell^{g\mu} = \int \frac{d\chi}{\chi^2} q_g(\chi) q_\mu(\chi) P^{gm}(k_\ell, z), \quad (38)$$

$$C_\ell^{\mu\mu} = \int \frac{d\chi}{\chi^2} q_\mu^2(\chi) P^{mm}(k_\ell, z), \quad (39)$$

$$C_\ell^{g\kappa,0} = \int \frac{d\chi}{\chi^2} q_g(\chi) q_\kappa(\chi) P^{gm}(k_\ell, z), \quad (40)$$

$$C_\ell^{\mu\kappa} = \int \frac{d\chi}{\chi^2} q_\mu(\chi) q_\kappa(\chi) P^{mm}(k_\ell, z). \quad (41)$$

The magnification bias correction is usually negligible for the C_ℓ^{gg} power spectrum, as the additional terms are small compared to the $C_\ell^{gg,0}$ term (due to the small overlap in kernels q^g and q^μ). It can however sometimes be of comparable amplitude in the cross-correlation $C_\ell^{g\kappa}$, as the q_κ and q_μ kernels can have significant overlap – both represent lensing effects from structures on the line of sight. We will include these contributions when modelling the power spectra, both for gg and $g\kappa$, but we will ignore the contribution from magnification to the projected bispectrum. This is justified since, as in the case of C_ℓ^{gg} , the contribution from magnification to $\Phi_{LL\ell}^{ggg}$ is likely small. Although this may not be the case for $\Phi_{LL\ell}^{g\kappa\kappa}$ in general, the relatively small signal-to-noise ratio with which we are able to measure this correlation on the scales we will use for cosmological inference makes the contribution from magnification irrelevant.

2.5. Inference pipeline

To quantify the additional information brought about by the projected bispectrum, in Section 4.2 we will use our measurements to derive rudimentary constraints on cosmological parameters. To do so, we will use a Gaussian likelihood of the form

$$-2 \log p(\mathbf{d}|\vec{\theta}) = (\mathbf{d} - \mathbf{t}(\vec{\theta}))^T \mathbf{C}^{-1} (\mathbf{d} - \mathbf{t}(\vec{\theta})) + \mathcal{K}. \quad (42)$$

Here, \mathbf{d} is the data vector containing our combined measurements of the power spectra and bispectra (however we will see in Section 4.2 that the $gg\kappa$ bispectrum will ultimately not be included in the data vector), and \mathbf{C} is the covariance matrix of those measurements, which is obtained as described in sections 2.1.3, 2.2, and Appendix C. The theory predictions $\mathbf{t}(\vec{\theta})$ are generated for a set of parameters $\vec{\theta}$ as described in Section 2.4, and \mathcal{K} is an irrelevant normalisation constant, independent of $\vec{\theta}$.

The parameter set in our study is relatively small, containing only σ_8 , Ω_m , and the linear bias b_1 . All other cosmological parameters are simply fixed to the best-fit values found by Planck Collaboration et al. (2020a). The higher-order bias parameters, b_2 and b_s will be determined in terms of b_1 : in our fiducial analysis, we will make use of the empirical relations between these parameters and b_1 found in Lazeyras et al. (2016) and Lazeyras & Schmidt (2018). We will refer to these as the ‘‘coevolution relations’’ in what follows. These relations have been found to accurately describe the clustering of dark matter haloes as well as galaxies – although with a much larger scatter in the latter case (Barreira et al. 2021). Our purpose with these simplifications is to test the constraining power of the projected galaxy bispectrum through a simple cosmological analysis. We leave a more detailed analysis, in which the higher-order bias parameters are determined self-consistently by including their contribution to the one-loop power spectra, and which incorporates external data to place priors on the cosmological parameters we fix here, for future work.

We infer parameters from this likelihood using the Markov Chain Monte-Carlo (MCMC) technique, with the affine-invariant sampler implemented in emcee (Foreman-Mackey et al. 2013), and we use the Core Cosmology Library (CCL⁶) (Chisari et al. 2019) to carry out most of the theory calculations described below. Generating analytical predictions for

⁶ <https://github.com/LSSTDESC/CCL>

Parameter	Fiducial value	Prior
$\Omega_{\text{CDM}}^{\text{fid}}$	0.2607	
Ω_b^{fid}	0.049	
h^{fid}	0.6766	
σ_8^{fid}	0.8102	
n_s^{fid}	0.9665	
b_1	1	$\mathcal{U}[0, 6]$
$r_{\sigma_8} = \sigma_8^{\text{fid}} / \sigma_8$	1	$\mathcal{U}[0, 2]$
$\Omega_m = \Omega_{\text{CDM}} + \Omega_b^{\text{fid}}$	$\Omega_{\text{CDM}}^{\text{fid}} + \Omega_b^{\text{fid}}$	$\mathcal{U}[0.05, 0.5]$

Table 1

Fiducial cosmological parameters, corresponding to the values favoured by Planck (Planck Collaboration et al. 2020a), and parameter priors used in our inference pipeline. For convenience we directly sample r_{σ_8} , the ratio of σ_8 to its fiducial value, and instead of sampling Ω_m directly, we vary Ω_{CDM} while keeping Ω_b fixed to its fiducial value. We denote a uniform distribution between values a and b using the shorthand $\mathcal{U}[a, b]$.

the FSB can be computationally costly, given the relatively large numbers of triangle configurations corresponding to a given $\Phi_{LL\ell}$, and the need to perform the convolution in Eq. 5. Doing so on the fly at every step in an MCMC chain can be prohibitively expensive. We solve this problem by taking advantage of the simple scaling of the FSB and the power spectrum as functions of the model parameters (particularly b_1 and σ_8). Specifically, in the case of the FSB:

1. We generate the perturbation theory, quadratic and tidal terms templates (the terms in round brackets in Eqs. 29 and 30) for a fixed cosmology, with parameters given in Table 1. To decrease computation time when calculating the projected bispectrum and transforming it into the FSB, we create interpolators for each of these theoretical templates at the level of the projected bispectrum, computing them on a 3D grid of predefined multipoles. These are then used to evaluate the bispectrum at every integer (ℓ_1, ℓ_2, ℓ_3) and transforming it into the FSB via Eq. 5. All bias parameters are set to 1 when generating these templates.
2. We also generate templates for the different terms entering the galaxy-galaxy and galaxy-convergence power spectra, including all contributions from magnification (see Eqs. 35 and 36).
3. To account for the dependence on Ω_m we simply repeat the previous two steps for 100 different values of this parameter, spanning the range $\Omega_m \in [0.05, 0.5]$, and generate a cubic spline interpolator for each FSB component as a function of Ω_m . We provide an overview of the final interpolator performance, both in terms of runtime and accuracy, in Appendix D.
4. To generate predictions for a cosmology with a different value of σ_8 and Ω_m , we simply rescale each of the templates described above, evaluated at the corresponding value of Ω_m , by appropriate powers of the ratio $r_{\sigma_8} \equiv \sigma_8 / \sigma_8^{\text{fid}}$, where σ_8 is the sampled value of this parameter, and σ_8^{fid} is the fiducial value (given in Table 1). The ggg and $g\kappa\kappa$ bispectra both scale with $r_{\sigma_8}^4$,

with the exception of the shot noise terms proportional to the power spectrum, which are scaled as $r_{\sigma_8}^2$, and the pure noise term in Eq. 31 which is independent of σ_8 . In turn, all terms entering the gg and $g\kappa$ power spectra scale with $r_{\sigma_8}^2$.

- Finally, each bispectrum template is scaled by the right factors of (b_1, b_2, b_s) , given in Eqs. 29 and 30. In the case of the power spectrum, the template $C_\ell^{gg,0}$ is scaled with b_1^2 , while the templates $C_\ell^{g\kappa,0}$ and $C_\ell^{g\mu}$ are simply multiplied by b_1 . This also applies to the shot-noise contributions to the bispectrum (Eqs. 31 and 32).

With this approach, each evaluation of the likelihood is relatively fast, allowing us to explore the constraining power of different combinations of power spectra and FSB terms. We reiterate that our model is relatively simple, including terms only at the tree level in both the power spectrum and bispectrum, and using empirical relations to connect the different bias parameters. The analysis presented here is thus only intended to represent a first exploration of the detectability of the projected bispectrum through the FSB approach, its qualitative agreement with theoretical expectations, and its constraining power. As such, the results presented here should be interpreted with a pinch of salt. A more rigorous cosmological analysis of these data is currently in progress and will be presented in future work (Verdiani et al. 2025).

To ensure that our theoretical model is valid, we introduce scales cuts in the data vector: we only select scales below $\ell_{\max} = \chi(\bar{z})k_{\max}$, where \bar{z} is the effective redshift of the galaxy sample. The value of k_{\max} depends on the observable: we set $k_{\max}^P = 0.07 \text{ Mpc}^{-1}$ for the power spectrum, and a more conservative $k_{\max}^B = 0.05 \text{ Mpc}^{-1}$ for the bispectrum. The value of k_{\max}^P matches that used by Sailer et al. (2025b) in the analysis of the LRG sample used here assuming a linear bias relation. Although the tree-level matter bispectrum usually provides accurate fits to simulation results for scales up to $k_{\max} \lesssim 0.1 h\text{Mpc}^{-1}$ (see e.g. Takahashi et al. 2020), our k_{\max}^B cuts are motivated by Ivanov et al. (2022), where a scale cut $k_{\max} = 0.08 h\text{Mpc}^{-1}$ is used to model the tree-level bispectrum model in redshift space at $z = 0.61$ (which lies between the first and second redshift bins used here, see Section 3.1). For our fiducial cosmology described in Table 1, this cut corresponds to about $k_{\max}^B = 0.05 \text{ Mpc}^{-1}$, which in turn gives $\ell_{\max}^P = 130, 166, 200, 226$ and $\ell_{\max}^B = 93, 119, 143, 161$ in the four redshift bins studied here. We do not expect these conservative cuts to vary greatly for similar values of σ_8 or h . Note that this conservative k_{\max}^B cut was necessary in Ivanov et al. (2022) due to the presence of Redshift-Space Distortions (RSDs), which do not affect 2D projected probes as much as their 3D counterparts. It is likely that this scale cut is thus conservative for our purposes, and determining the smallest physical scale up to which projected bispectra may be described by simple perturbation theory models would allow us to improve upon any constraints derived in this analysis.

The scale cut applies to all three legs (ℓ_1, ℓ_2 and ℓ_3) of the bispectrum, and therefore we must make sure that their values satisfy $\ell_i < \ell_{\max}^B$. Such scale cuts are straightforward to implement thanks to the filtering operation introduced in the FSB estimator. Given that two of the legs (ℓ_1 and ℓ_2) can only belong to the scales selected by the filter L , one must choose filters that remain below the designated ℓ_{\max}^B , such

that $\max(\{\ell \in L\}) < \ell_{\max}^B$. If that condition is satisfied, we can then apply the usual scale cuts on the remaining leg ℓ_3 , only keeping values of $\Phi_{LL\ell}$ which satisfy $\ell < \ell_{\max}^B$. These scale cuts would be difficult to implement on a regular skew-spectrum (i.e. in the absence of filtering before squaring the field): once the projected bispectrum is compressed along one dimension, individual triangle contributions cannot be differentiated.

The final scale cut applied on the FSB is the minimum ℓ_{\max} set by either k_{\max}^B or by the triangle inequality: the FSB filter used imposes a limit on the triangle configurations contributing to the estimator – specifically, there cannot be contributions beyond twice the upper limit of the filter (we only keep values of $\Phi_{LL\ell}$ that satisfy $\ell < 2 \max(\{\ell \in L\})$).

As described in Eq. 42, we approximate the likelihood of the data vector \mathbf{d} to a multivariate normal distribution, described by the data vector covariance \mathbf{C} . This is usually a reasonable approximation at high ℓ where the Central Limit Theorem (CLT) applies, but can fail at the largest scales; we therefore apply another fiducial low- ℓ cut at $\ell_{\min} = 20$ for all measured observables – $\Phi_{LL\ell}^{ggg}, \Phi_{LL\ell}^{g\kappa}, C_\ell^{gg}$ and $C_\ell^{g\kappa}$. This should also help mitigate any large-scale inaccuracies introduced by the Limber approximation and neglecting RSD contributions to both FSBs – although the filter used to define the FSB does include large scales, below ℓ_{\min} , in the bispectrum. As shown in Verdiani et al. (2025), however, the larger statistical uncertainties in this statistic makes these effects negligible. H25 furthermore showed that $\Phi_{LL\ell}^{ggg}$ and C_ℓ^{gg} in fact follow a near-Gaussian distribution, even for bandpowers including lower multipoles ($\ell > 2$).

We use uninformative top-hat priors for the three free parameters of our model ($\{\sigma_8, \Omega_m, b_1\}$). These are listed in Table 1. All other cosmological parameters are fixed to the best-fit *Planck* values (Planck Collaboration et al. 2020a), also listed in the table.

2.6. Estimating detection significance

To quantify the detection of a potential bispectrum signal in our measurements, we compute the Signal-to-Noise ratio (hereafter SNR), approximately given by

$$\text{SNR} = \sqrt{\chi_0^2 - N_{\text{dof}}}, \quad \chi_0^2 \equiv (\mathbf{x} - \boldsymbol{\mu})^\top \mathbf{C}^{-1} (\mathbf{x} - \boldsymbol{\mu}), \quad (43)$$

where \mathbf{x} is one FSB measurement, $\boldsymbol{\mu}$ is the expectation value of the estimator for a null detection – in our case, the noise terms given by either Eq. 31 or 32. The covariance matrix \mathbf{C} is calculated as described in Section 2.1.3. N_{dof} is the number of degrees of freedom, in this case the number of data points in \mathbf{x} , and represents the expectation value of the previous term in the case of pure noise fluctuations. This method constitutes a good first estimate of the SNR, in that it does not depend on any specific model for the signal we are after. When the SNR is sufficiently high, the argument of the square root is always positive, as $\chi_0^2 \gg N_{\text{dof}}$. In low-SNR scenarios, noise fluctuations may make the argument of the square root negative. In such cases, we will simply report $\text{SNR} = 0$. We will refer to this first model-independent estimate of the SNR as “SNR₁” in what follows.

Another way to compute the SNR would be to fit our measurements to a best-guess template of the expected signal with a free amplitude, and to quantify the significance with which this amplitude differs from zero. As a best-guess template \mathbf{T} we use the theory predictions described in Section 2.4.3, using

either the fiducial parameter values (Tables 1 and 2) in Section 4.1 or the best-fit model parameters found in Section 4.2.3. Scaling this template by a free amplitude A (i.e. $\mathbf{t} = A\mathbf{T}$), its best-fit and standard deviation can be estimated via generalised least-squares. The result can then be used to estimate the SNR of a given data vector \mathbf{x} :

$$\text{SNR} = \frac{A_{\text{best}}}{\sigma_A} = \frac{\mathbf{T}^T \mathbf{C}^{-1} (\mathbf{x} - \boldsymbol{\mu})}{\sqrt{\mathbf{T}^T \mathbf{C}^{-1} \mathbf{T}}}. \quad (44)$$

Note that here \mathbf{T} contains only the bispectrum signal (i.e. the FSB version of Eq. 29 or 30), with the noise components absorbed in $\boldsymbol{\mu}$, as in Eq. 43. We will refer to this second SNR estimate as ‘‘SNR₂’’ in what follows. It is worth noting that this SNR estimate is only as accurate as the model used to construct \mathbf{T} which, as we discussed in the previous section, may not be the case on small scales ($\ell \geq \ell_{\text{max}}^B$).

3. DATA

3.1. DESI LRGs

We study the clustering of photometric luminous red galaxies (LRGs) found in the 9th data release of the DESI Legacy Imaging Survey (Dey et al. 2019; Zhou et al. 2023a). The specific sample used here is described in Zhou et al. (2023b), and was used by White et al. (2022) (and more recently by Sailer et al. 2025b) to extract cosmological constraints from their two-point angular clustering and cross-correlation with CMB lensing data.

The sample is divided into four different redshift bins, covering the redshift range $0.4 \lesssim z \lesssim 1$, with number densities in the range $\bar{n} \sim 80\text{--}160 \text{ deg}^{-2}$. We use the maps of the LRG overdensity in each redshift bin used in White et al. (2022), and made publicly available⁷ together with the analysis mask. We note that changes were made to the sample used in White et al. (2022), as described in Zhou et al. (2023b), and this revised sample was then used in the cosmological analysis of Sailer et al. (2025b). As explained in Zhou et al. (2023b), the main changes made involve an improvement in the redshift distributions, modifications to the zero-point offsets in the southern sky, and changes in the sky contaminant templates used. This results in a small change in the LRG auto-correlations ($< 2\%$). We have verified that none of our FSB measurements (neither $\Phi_{LL\ell}^{ggg}$ nor $\Phi_{LL\ell}^{ggk}$) change significantly within the measurement uncertainties when using the newer sample. Hence, none of the results presented here, regarding the detectability and constraining power of the projected bispectrum, should be affected by these changes.

We refer to each of the four redshift bins as z_i , with $i \in [1, 4]$. The shot-noise levels, linear galaxy bias, and estimated number counts slope s , were presented in Table 1 of White et al. (2022). We repeat them in Table 2 for convenience. We use the values of s reported in this table to estimate the contribution from magnification bias to the measured power spectra.

3.2. Planck

We use maps of the CMB lensing convergence κ constructed from the temperature and polarisation maps of the *Planck* experiment. In particular, we use the κ maps presented in Planck Collaboration et al. (2020b), reconstructed from the *Planck*

⁷ <https://zenodo.org/records/5834378>

Bin	\bar{z}	\bar{n}	$10^6 N^{gg}$	s	b_1	ℓ_{max}^P	ℓ_{max}^B
z_1	0.47	83	4.02	0.982	1.9	130	93
z_2	0.63	149	2.24	1.033	2.1	166	119
z_3	0.79	162	2.07	0.961	2.4	200	143
z_4	0.92	149	2.26	1.013	2.5	226	161

Table 2

Properties of the LRG samples used in this analysis. Most of these are taken from Table 1 of White et al. (2022). They include the mean redshift of each sample \bar{z} , the mean number of galaxies per square degree \bar{n} , the shot-noise amplitude N^{gg} , the number counts slope s used to estimate the impact of magnification bias, and the inferred large-scale Eulerian bias b_1 . We also list the small-scale cuts used in our analysis of the power spectrum ℓ_{max}^P and bispectrum ℓ_{max}^B .

2018 (PR3) data release maps. In particular we use the minimum variance (MV) κ map, which combines information from temperature and polarisation. These data are processed as described in White et al. (2022): the public harmonic coefficients $\kappa_{\ell m}$ are first band-limited and transformed into a HEALPix map, and the analysis mask is apodised with a 0.5° kernel to reduce the statistical coupling between adjacent multipoles in the estimated power spectra.

As noted in Farren et al. (2024); Kim et al. (2024); Sailer et al. (2025b), masking, filtering, and specific analysis choices in lensing reconstruction affect the effective normalisation of the reconstructed κ map in an inhomogeneous manner. This may be corrected via Monte-Carlo simulations (and hence the associated transfer function is often called the ‘‘MC correction’’), but the correction depends on the sky patch under study, and must therefore be recalculated for each cross-correlation. As shown in Sailer et al. (2025b), this correction is at the level of $\sim 1\%$ of C_ℓ^{gk} in the case of the LRG sample used here, and including it leads to a $\sim 0.5\sigma$ downwards shift in the value for the amplitude of matter fluctuations recovered by combining information from all redshift bins (corresponding to a $\sim 0.3\sigma$ shift in the case of the per-bin constraints we report in Section 4.2). Since this is commensurate with the impact of other analysis choices, including the treatment of neutrino masses and volume effects (see Sailer et al. 2025b), we chose not to apply this correction to C_ℓ^{gk} in this analysis, for simplicity and in order to facilitate the comparison with the results in White et al. (2022). Furthermore, the impact of this correction on the new measurement of $\Phi_{LL\ell}^{ggk}$ presented here is entirely negligible, given the significantly lower SNR of this measurement compared to C_ℓ^{gk} (see Section 4.1).

4. RESULTS

In this section, we report the detection of the galaxy bispectrum in all redshift bins introduced in Section 3.1, as well as the detection of the galaxy-convergence bispectrum in three out of the four redshift samples. We also discuss the constraining power of the galaxy and galaxy-convergence bispectra, and provide the first (albeit rudimentary) cosmological constraints on the clustering amplitude σ_8 and the matter density Ω_m combining power spectra and the projected galaxy bispectrum.

4.1. Measurement and detection

We measure the FSBs using the estimator described in Sections 2.1 and 2.2, using the filters and bandpowers described in Section 2.3. We generate basic theoretical predictions (Section

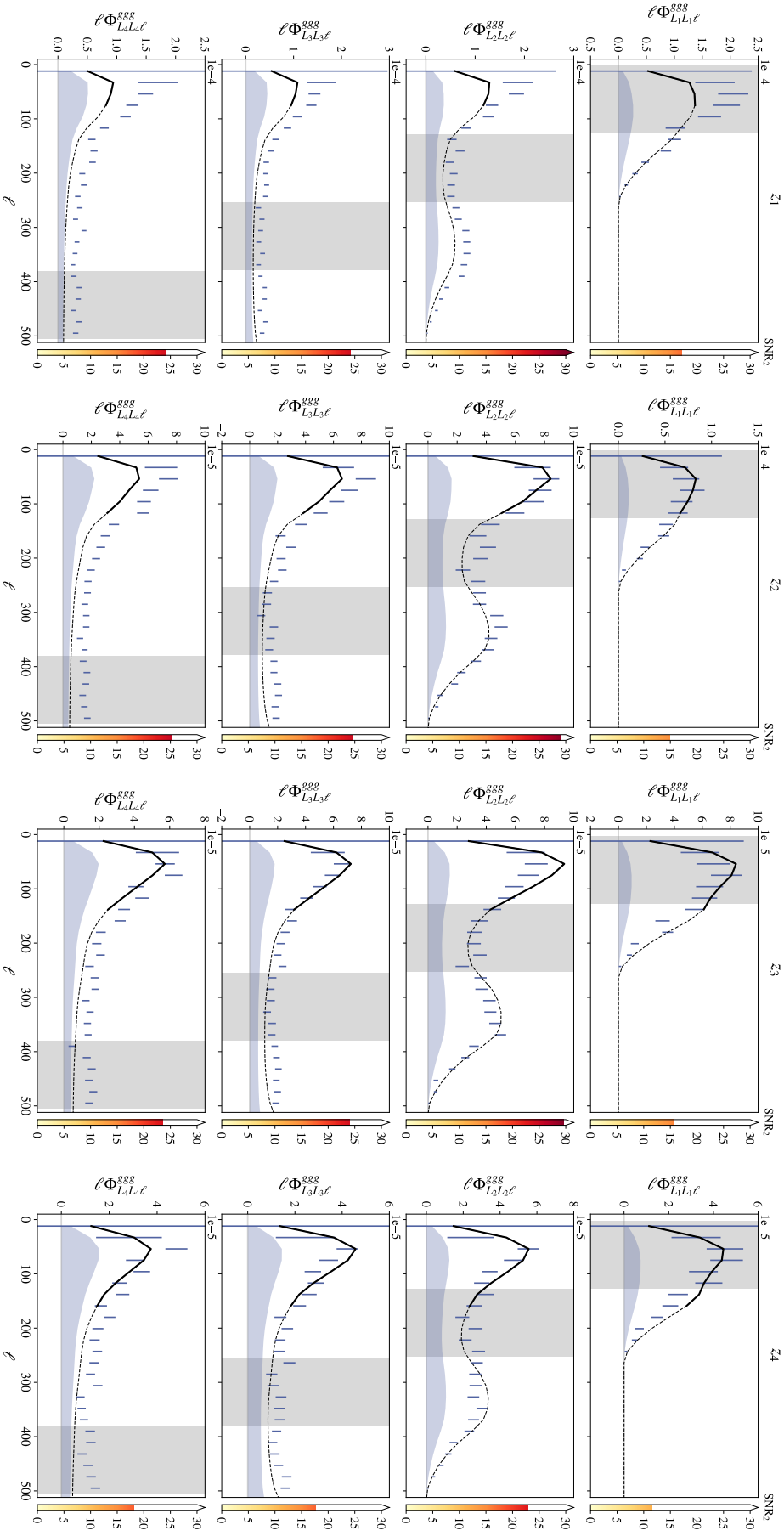


Figure 2. The ggg FSBs measured in all four redshift bins. Each column corresponds to one redshift bin, and each row to one of the four colourful filters shown in Fig. 1 – here represented by the greyed-out band. The FSB measurements are shown in blue, and the black solid line shows the theoretical fit for published values of b_1 (White et al. 2022) and for a fiducial cosmology (Table 1). These theory predictions are used as templates in Eq. 44 to report the SNR₂ shown on the colour bars on the right of each FSB. Beyond the conservative cuts used in our inference pipeline (see Section 4.2), we show the predictions as dashed lines to emphasise that the tree-level bispectrum is not necessarily a good theoretical description of the power at those scales. It is worth noting that the FSBs in all but the first filter (i.e. the first row in this plot) also lie in this small-scale regime. The blue shaded area represents the amount of noise (Eq. 31) contributing to the overall theory prediction. Note that we plot $\ell\Phi_{LLL}^{ggg}$ instead of Φ_{LLL}^{ggg} to improve readability at higher multipoles.

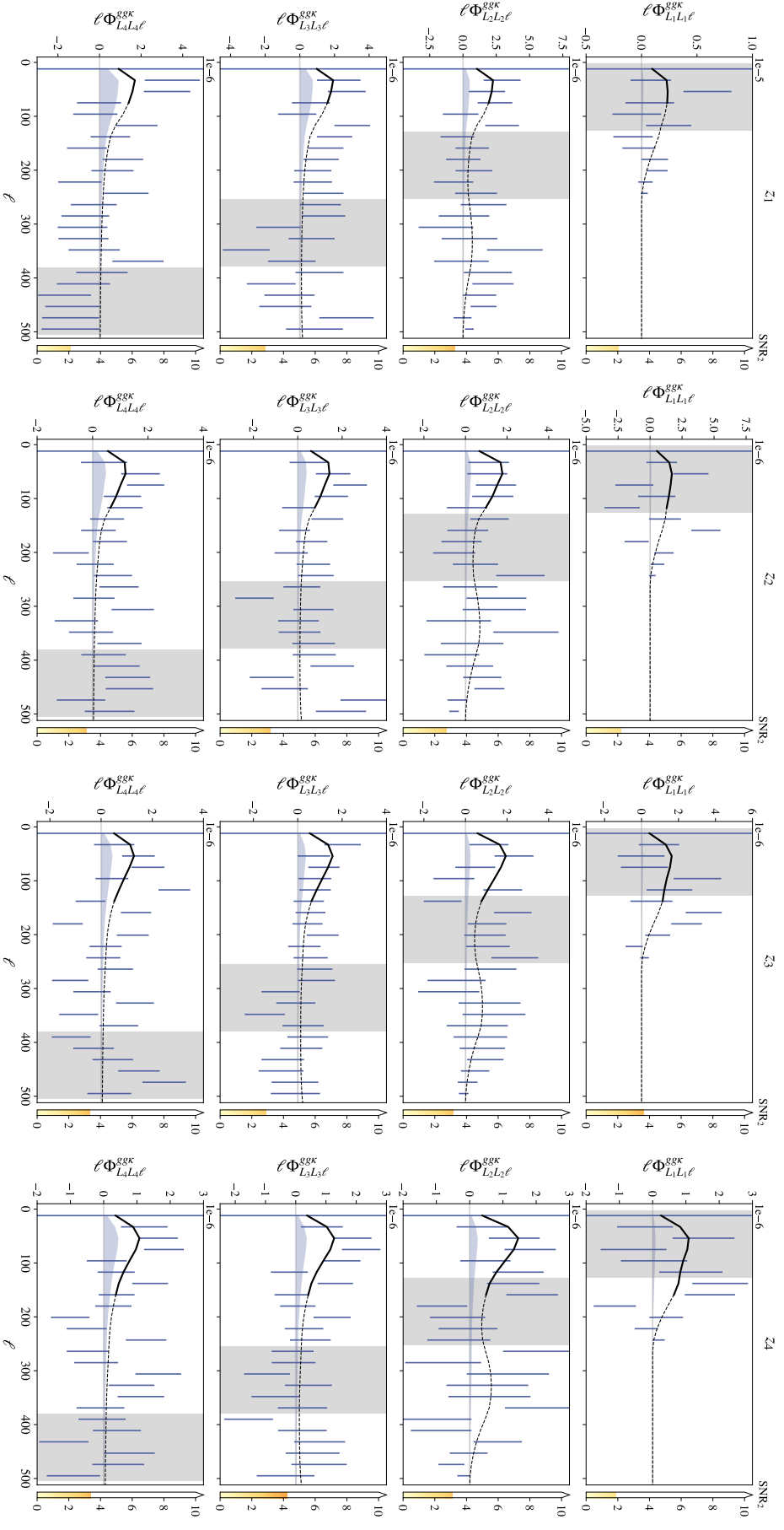


Figure 3. The ggk FSBs measured in all four redshift bins. Each column corresponds to one redshift bin, and each row to one of the four colourful filters shown in Fig. 1 – here represented by the greyed-out band. The FSB measurements are shown in blue, and the black solid line shows the theoretical fit for published values of b_1 (White et al. 2022) and for a fiducial cosmology (Table 1). These theory predictions are used as templates in Eq. 44 to report the SNR₂ shown on the colour bars on the right of each FSB. Beyond the conservative cuts used in our inference pipeline (see Section 4.2), we show the predictions as dashed lines to emphasise that the tree-level bispectrum is not necessarily a good theoretical description of the power at those scales. The blue shaded area represents the amount of noise (Eq. 32) contributing to the overall theory prediction. Note that we plot $\ell\Phi_{LLL}^{ggk}$ instead of Φ_{LLL}^{ggk} to improve readability at higher multipoles.

2.4.3) for these FSBs by rescaling the bispectrum templates according to the method laid out in Section 2.5. These were generated using the values of the linear bias found in White et al. (2022) (see Table 2), calculating the quadratic and tidal bias parameters using the coevolution relations, and setting all cosmological parameters to the best-fit values found by *Planck* (see Table 1). The resulting measurements of $\Phi_{LL\ell}^{ggg}$ and $\Phi_{LL\ell}^{gg\kappa}$, together with these theoretical predictions, are shown in Figs. 2 and 3, respectively. In each panel, the blue shaded band shows the contribution from shot noise, the vertical gray band marks the filter used to calculate the FSB, and the vertical colour bar shows the SNR with which the signal is detected, which we discuss below.

We expect the tree-level description of the galaxy bispectrum to be reliable when all three legs (ℓ_1, ℓ_2, ℓ_3) remain below the fiducial multipole cuts we describe in Section 2.5. This regime corresponds to only a subset of Figs. 2 and 3:

- Only the first filter selects scales (ℓ_1, ℓ_2) below these scale cuts, whereas the three other filters select smaller scales where linear perturbation does not necessarily hold;
- We show the predictions as bold dark lines where ℓ_3 (which corresponds to the x-axis) falls below the aforementioned scale cuts, and as dashed lines beyond.

Therefore, our theoretical predictions should be most reliable in the first row of each figure, and where theoretical predictions are shown in bold. The naive theoretical expectation, with no free parameters, provides a reasonable description of the *ggg* FSBs within these limits for all except in the first redshift bin, where it systematically underpredicts the signal. As we discuss in Section 4.2.2, this can be accommodated by the combination of a higher value of the linear bias and a lower σ_8 (the latter in qualitative agreement with the lower clustering amplitude seemingly preferred by this sample in White et al. 2022). Interestingly, the theoretical predictions are surprisingly accurate even beyond these scale cuts: in the first and second row of Figs. 2 and 3, the tree-level bispectrum still provides a somewhat reasonable fit to the measurements over an extended multipole range. It would be interesting to determine the range of scales over which the projected bispectrum can be safely predicted. Since the projected galaxy overdensity is necessarily more Gaussian than its 3D counterpart, it may be possible to extend the analysis to smaller angular scales, thereby recovering more cosmological information. We leave this study for future work. For now we will remain cautious and implement conservative scale cuts for the analysis in Section 4.2. However, to quantify the significance with which the bispectrum signal is detected in these measurements, independently of our ability to accurately model it, we will use the full range of scales $\ell < 2N_{\text{side}}$. Visually, the detection of the non-Gaussian contributions to the FSB can be seen by comparing our measurements with the blue band showing the expected contribution from shot noise.

The SNR with which the *ggg* and *gg κ* FSBs are detected in each redshift bin, combining the signal from all FSB filters, are reported in Table 3. The combined SNR is computed following the two methods described in Section 2.6, using as input the concatenated data vector containing the FSB measurements in all filters. We use the theoretical predictions shown in Figs. 2 and 3 (or rather their pure signal contributions) to build the theoretical template used to estimate SNR_2 . It is worth noting that, since the theoretical template is not accurate on small

Bin	FSB type	SNR_1	SNR_2
z_1	<i>ggg</i>	45.06	38.37
	<i>ggκ</i>	2.39	3.53
z_2	<i>ggg</i>	43.82	39.27
	<i>ggκ</i>	6.06	4.60
z_3	<i>ggg</i>	43.65	40.08
	<i>ggκ</i>	7.45	5.44
z_4	<i>ggg</i>	33.58	30.70
	<i>ggκ</i>	6.50	5.04

Table 3

Combined SNRs corresponding to the FSBs shown in Figs. 2 and 3.

scales (this is clearly visible in the figures as the FSB filter moves to higher ℓ s and higher filters – as seen also in H25), the approach used to estimate SNR_2 may become unreliable. Thus, we also provide the estimates of SNR_1 , which do not rely on any theoretical template (but instead become unreliable for low-SNR data).

The detection of the *ggg* FSB is indisputable, with a combined $\text{SNR} > 30$ in all redshift bins. We find that both estimates, SNR_1 and SNR_2 are in qualitative agreement, with SNR_1 providing a consistently larger estimate (by ~ 10 -20%). This is likely due to the fact that the model used to create the theoretical template **T** used to calculate SNR_2 (see Eq. 44) under-predicts the signal on small scales, leading to a lower inferred signal amplitude.

In turn, the SNR of the *gg κ* FSBs is significantly lower. Nevertheless, the signal is clearly detected, with $\text{SNR} > 5$ in the three last redshift bins, and only tentatively in the first bin ($\text{SNR} \sim 3$). Judging from Fig. 3, much of the signal seems to be concentrated in the higher- ℓ filters, which will not be used in the cosmological analysis presented in the next section. Thus, although detected, we do not expect $\Phi_{LL\ell}^{gg\kappa}$ to contribute significantly to the final cosmological constraints.

4.2. Constraining power

4.2.1. FSB measurements

As described in Section 2.5, we implement conservative scale cuts to the data to ensure our theoretical predictions are reliable. This means we must also make sure the FSB filters chosen are such that all triangle configurations contributing to the estimator satisfy these cuts. As described in Section 2.3, to ensure this, we use new measurements of the FSB, using a single filter lying below the most conservative ℓ_{max}^B cut (corresponding to the lowest redshift bin z_1 , shown in Fig. 1), and reduce the bandpower width to $\Delta\ell = 9$. Our data vector, for a given redshift bin, will therefore consist of a single $\Phi_{LL\ell}^{ggg}$ and $\Phi_{LL\ell}^{gg\kappa}$ for this filter, in addition to the power spectrum measurements C_ℓ^{gg} and $C_\ell^{g\kappa}$. These measurements are shown in Fig. 4 for the four redshift bins, truncated at their respective ℓ_{max} cuts. Unsurprisingly, as discussed in the previous section, the SNR of the $\Phi_{LL\ell}^{gg\kappa}$ measurements within these scales is very low (below 1 in all cases). We will therefore discard the *gg κ* measurements in our analysis, keeping only the *ggg* FSBs, which are detected above 6σ in all cases. Increasing the SNR should allow us to make the most of the constraining power

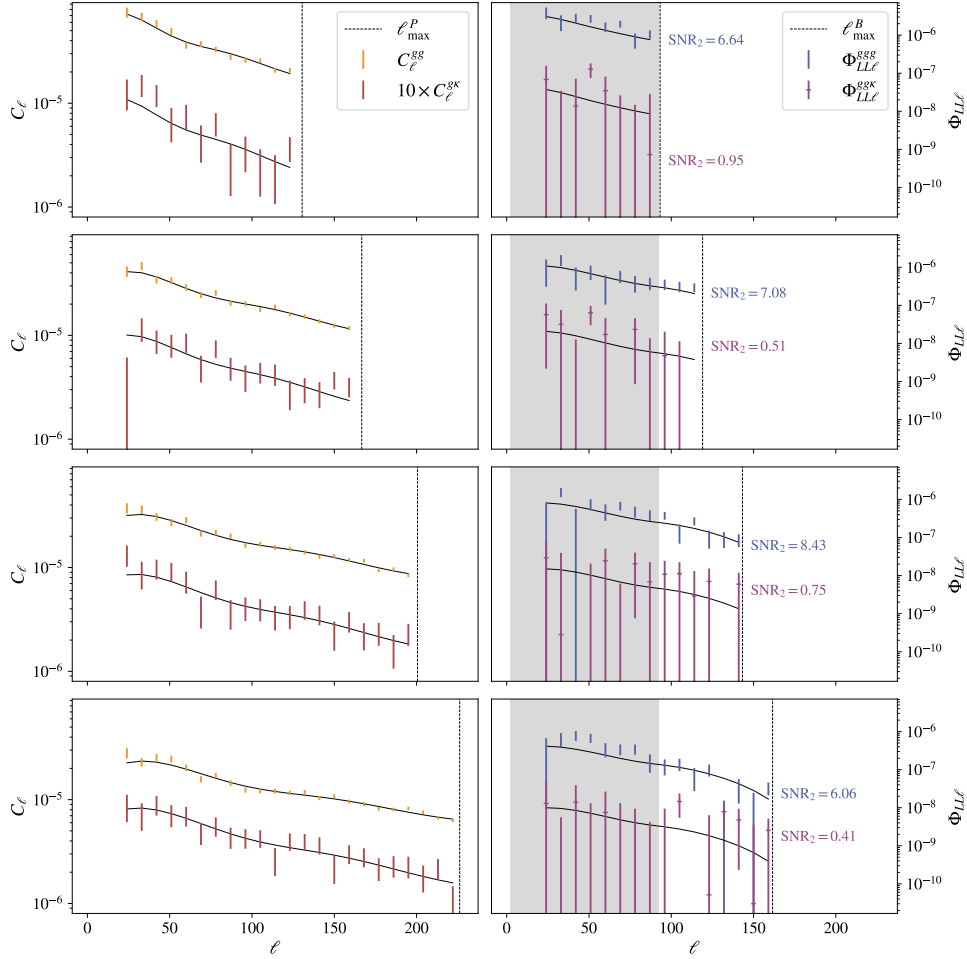


Figure 4. A visual representation of the data vectors used to derive constraints on σ_8 and Ω_m , with power spectra C_ℓ^{gg} (yellow data points) and C_ℓ^{gk} (red, multiplied by a factor of 10 for readability) measurements on the left, and FSBs $\Phi_{LL\ell}^{ggg}$ (blue) and $\Phi_{LL\ell}^{gk}$ (purple) on the right. Each row corresponds to a different redshift bin, starting from lowest redshift at the top. The multipole cuts evolve accordingly (the number of data points included in the analysis thus increases with redshift). The new filtered range (for a comparison with previous filters, see Fig. 1) is shown in grey, and fits within the most restrictive ℓ_{\max}^B cut (lowest redshift bin). The black lines show theory predictions for the best-fit values obtained from constraining the models with the full data vector, $\Phi_{LL\ell}^{ggg} + C_\ell^{gg} + C_\ell^{gk}$. These best-fit values are reported in Table 4, and the corresponding predictions are used as templates to report SNR_2 (Eq. 44) indicated next to each FSB.

of the gk FSBs. This could be achieved by either exploiting all scales within the studied multipole range (allowing for the filter to be defined up to $\ell_{\max}^B(z)$ in each bin, instead of using the same, large-scale filter for all) or pushing our model to smaller scales (thus allowing us to relax the conservative scale cuts used so far in this study). Using more sensitive CMB lensing data, from ground-based experiments such as the Atacama Cosmology Telescope (Madhavacheril et al. 2024), could also improve the SNR of these measurements. We will study these potential avenues for optimisation in future work.

We also add in Fig. 4 the best-fit theoretical predictions given by the constraints obtained in Section 4.2.3 for the combined probes $\Phi_{LL\ell}^{ggg}$, C_ℓ^{gg} , and C_ℓ^{gk} . As we will quantify in Section 4.2.3, these provide an excellent fit to our measurements over all the scales studied.

4.2.2. Probe complementarity

As a pedagogical detour, before presenting a cosmological analysis of the data vector presented in the last section, let us study the ability of the galaxy bispectrum to break parameter degeneracies and improve cosmological constraints. To do so, let us use a simpler theoretical model in which we keep Ω_m fixed to its fiducial value (see Table 1), while varying both σ_8

and b_1 , the two parameters that affect the overall amplitude of the clustering statistics (both C_ℓ s and FSBs). For simplicity, we will also focus on the third redshift bin, z_3 , alone, where the ggg FSB has the highest SNR.

We can exploit the different dependence on b_1 and σ_8 of the power spectra and bispectra. For simplicity, and without loss of generality, let us ignore the contributions from magnification bias, as well as the bispectrum contributions dependent on the quadratic and tidal bias parameters. At the tree level, the amplitude of the different power spectra and FSBs considered here depends on σ_8 and b_1 as follows:

$$C_\ell^{gg} \propto \sigma_8^2 b_1^2, \quad C_\ell^{gk} \propto \sigma_8^2 b_1, \quad (45)$$

$$\Phi_{LL\ell}^{ggg} \propto \sigma_8^4 b_1^\alpha, \quad \Phi_{LL\ell}^{gk} \propto \sigma_8^4 b_1^\beta, \quad (46)$$

with $\alpha = 3$ and $\beta = 2$ ignoring contributions from b_2 and b_s . The complementary scaling with b_1 and σ_8 of these spectra makes it possible to constrain both parameters by combining any two of them⁸. In practice, however, the scaling of the FSB

⁸ Except for the combination of C_ℓ^{gk} and $\Phi_{LL\ell}^{gk}$, which constrain only the combination $\sigma_8^2 b_1$ in both cases. In this sense, the loss of the gk FSB due to its poor SNR is not a major setback for this analysis.

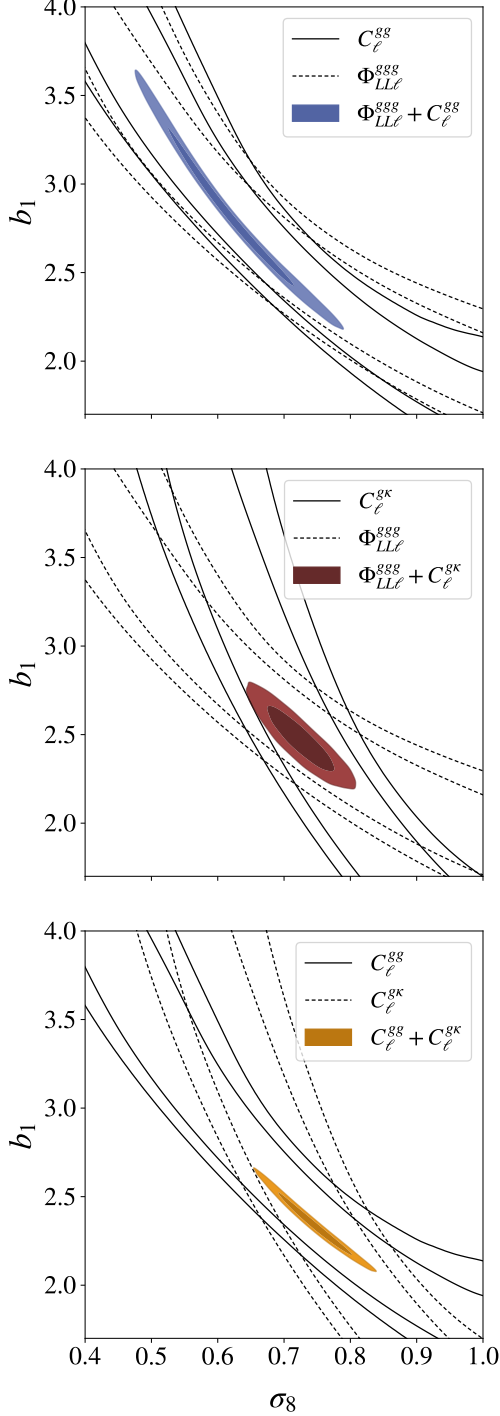


Figure 5. Constraints on σ_8 and b_1 from three data combinations: $\Phi_{LL\ell}^{ggg} + C_\ell^{gg}$ (blue contours in top panel), $\Phi_{LL\ell}^{ggg} + C_\ell^{gk}$ (red contours, middle panel), and $C_\ell^{gg} + C_\ell^{gk}$ (yellow contours, bottom panel). The black contours show the degeneracy directions of individual power spectrum or FSB measurements, with the filled contours showing the combined constraints. The constraints shown were obtained for redshift bin z_3 .

with b_1 is more complicated due to the non-linear bias contributions at tree level that are the same order of magnitude as the terms containing only b_1 . In the next section we will assume co-evolution relations, which express b_2 and b_s as a function of b_1 . In this case, we find that at the characteristic scale $\ell \sim 75$ the effective values of α and β in each of the redshift bins are $\alpha \simeq 4.5$, $\beta \simeq 3.1$, although in general these values are scale-dependent and sample-dependent. Given that co-evolution equations are good, but imperfect approximations, it is necessary to marginalize over all three bias parameters, perhaps with an informative prior on bias relations.

In general, for the FSB measurements to be sufficiently complementary to C_ℓ^{gg} and C_ℓ^{gk} in breaking parameter degeneracies, these scaling indices should be sufficiently different from $\alpha = 4$ and $\beta = 2$. Although our measurement of the ggk FSB is not sufficiently sensitive, we can exploit the ggg FSB to break degeneracies in the (σ_8, b_1) parameter plane using this rationale. Fig. 5 illustrates how, by combining $\Phi_{LL\ell}^{ggg}$ with either C_ℓ^{gg} or C_ℓ^{gk} , we are able to constrain σ_8 . For the third redshift bin, the resulting constraints on σ_8 are⁹:

$$\sigma_8 = 0.619_{-0.073}^{+0.066}, \quad \left(C_\ell^{gg} + \Phi_{LL\ell}^{ggg} \right), \quad (47)$$

$$\sigma_8 = 0.724 \pm 0.034, \quad \left(C_\ell^{gk} + \Phi_{LL\ell}^{ggg} \right), \quad (48)$$

$$\sigma_8 = 0.745 \pm 0.038, \quad \left(C_\ell^{gg} + C_\ell^{gk} \right). \quad (49)$$

In the top panel of Fig. 5 we can see that the degeneracy directions for C_ℓ^{gg} and $\Phi_{LL\ell}^{ggg}$ are similar, but not exactly parallel. As we just saw, this is because $\alpha \simeq 4.5$ is close to, but different from the value $\alpha = 4$ that would make both datasets equivalent in terms of their σ_8 - b_1 scaling. This allows us to obtain a measurement of σ_8 using the clustering of galaxies alone, albeit with an uncertainty that is approximately twice as large as that obtained in combination with C_ℓ^{gk} . Interestingly, the combination of $C_\ell^{gk} + \Phi_{LL\ell}^{ggg}$ is able to constrain σ_8 with a similar precision to the 2×2 -point combination (and in fact with 10% smaller uncertainties, likely due to the steeper scaling of the FSB with b_1 than C_ℓ^{gg}). The constraints obtained with these different data combinations are compatible with one another at the 1 - 2σ level, with the galaxy-only combination ($gg + ggg$) returning the lowest value of σ_8 . We remind the reader that these constraints must be interpreted with care, due to the overly simplistic nature of the model used: not only have we kept Ω_m constant, we have also assumed a fixed relationship between the non-linear bias parameters and b_1 which, as we have just seen, directly affect the scaling of the bispectrum amplitude that allows us to break parameter degeneracies. These constraints are provided here only to illustrate the complementary nature of the galaxy projected bispectrum.

These two new probe combinations ($C_\ell^{gg} + \Phi_{LL\ell}^{ggg}$ and $C_\ell^{gk} + \Phi_{LL\ell}^{ggg}$) have exciting advantages in terms of robustness to potential systematics. First, an independent measurement of σ_8 can be obtained in the absence of any lensing information, by combining $C_\ell^{gg} + \Phi_{LL\ell}^{ggg}$ (blue contours), thus circumventing lensing systematics altogether, and using only data that is sensitive to structure in a relatively narrow range of redshifts. The $C_\ell^{gk} + \Phi_{LL\ell}^{ggg}$ combination (red contours) is also useful, allowing us to test for the potential impact of systematics in the C_ℓ^{gg} measurements on the final constraints (assuming that

⁹ We report 68% confidence level intervals throughout.

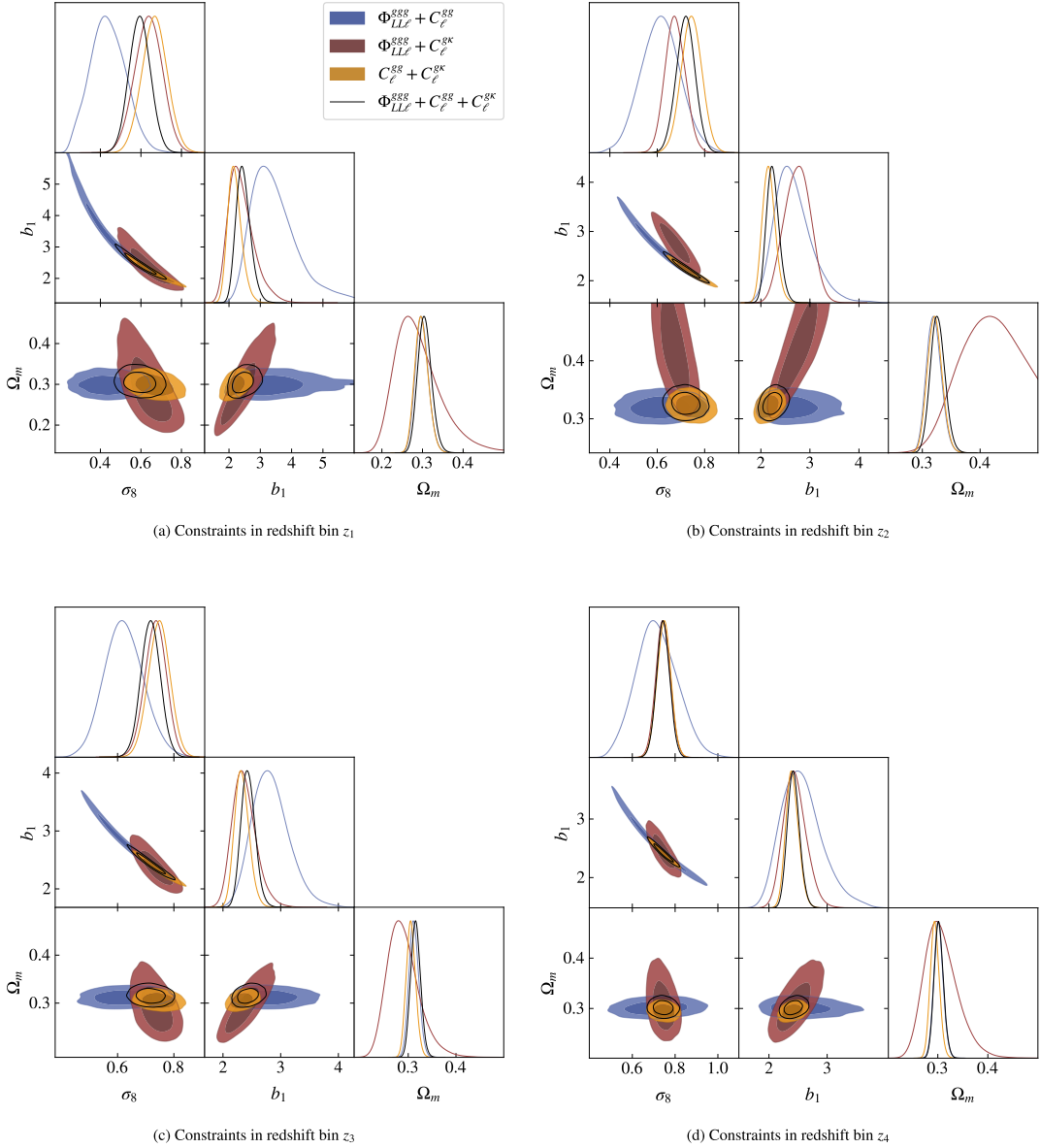


Figure 6. Constraints on σ_8 , Ω_m and b_1 found in the four different redshift bins. The yellow contours show constraints derived from the standard 2×2 -point combination, while the red and blue contours show two combinations of FSBs and power spectra which lead to additional constraints. The black contours show constraints obtained by combining all three probes ($C_\ell^{gk} + C_\ell^{gk} + \Phi_{LL\ell}^{gss}$). We only show the area of parameter space allowed by the priors.

systematic sky contamination in the galaxy overdensity maps would affect the 2- and 3-point correlators in different ways).

4.2.3. Constraints on σ_8 and Ω_m

Using the likelihood described in Section 2.5, we now derive constraints on σ_8 and Ω_m from different combinations of the measured power spectra and FSBs. We will present constraints found by analysing the data from each redshift bin independently. On the one hand, this simplifies the analysis, reducing the dimensionality of the parameter space to explore, and it allows us to study potential trends with redshift in the recovered cosmological parameters, and in the complementarity of the projected bispectrum. On the other hand, we do this to avoid reporting potentially unrealistic constraints, given the various simplifying assumptions used in this preliminary analysis. This will be addressed in future work.

The resulting constraints in the $(\sigma_8, \Omega_m, b_1)$ space found for each redshift bin are shown in Fig. 6. The blue, red, and yellow contours show the constraints found from the combinations $\Phi_{LL\ell}^{gss} + C_\ell^{gk}$, $\Phi_{LL\ell}^{gss} + C_\ell^{gk}$, and $C_\ell^{gk} + C_\ell^{gk}$, respectively. The numerical 68% confidence-level constraints on these parameters are listed in Table 4, which also lists the best-fit χ^2 value, and the associated probability-to-exceed (PTE) assuming a Gaussian likelihood with $N_{\text{dof}} = N_{\text{data}} - N_{\text{params}}$ degrees of freedom, where N_{data} is the size of the data vector, and $N_{\text{params}} = 3$ is the number of free parameters in our model. We find that the model provides a good description of the data in all cases, with PTE values ranging from 0.08 to 0.97. We again remind readers that these constraints should be interpreted in the context of the relative simplicity of the model used here, in which the power spectrum (and bispectrum) are only described at the tree level, and the non-linear bias pa-

Bin	Probe combination	b_1		σ_8		Ω_m		BF χ^2/N_{dof}	BF PTE
		BF	Mean	BF	Mean	BF	Mean		
z_1	$ggg + gg$	3.27	$3.46^{+0.44}_{-0.87}$	0.442	0.436 ± 0.086	0.296	$0.299^{+0.014}_{-0.017}$	17.0 / 17	0.45
	$ggg + g\kappa$	2.19	$2.40^{+0.27}_{-0.48}$	0.665	0.637 ± 0.067	0.259	$0.290^{+0.036}_{-0.067}$	14.87 / 17	0.6
	$gg + g\kappa$	2.14	$2.19^{+0.18}_{-0.25}$	0.676	0.668 ± 0.062	0.295	$0.298^{+0.015}_{-0.018}$	18.83 / 21	0.6
	$ggg + gg + g\kappa$	2.42	$2.46^{+0.19}_{-0.26}$	0.599	0.594 ± 0.052	0.303	$0.306^{+0.015}_{-0.018}$	29.13 / 29	0.46
z_2	$ggg + gg$	2.58	$2.67^{+0.26}_{-0.43}$	0.623	0.615 ± 0.083	0.318	$0.320^{+0.012}_{-0.014}$	12.63 / 24	0.97
	$ggg + g\kappa$	2.72	2.75 ± 0.26	0.679	0.676 ± 0.042	0.406	$0.414^{+0.057}_{-0.044}$	16.02 / 24	0.89
	$gg + g\kappa$	2.15	$2.17^{+0.12}_{-0.15}$	0.748	0.745 ± 0.044	0.320	$0.322^{+0.012}_{-0.013}$	22.68 / 29	0.79
	$ggg + gg + g\kappa$	2.23	$2.24^{+0.11}_{-0.14}$	0.723	0.720 ± 0.040	0.325	$0.327^{+0.012}_{-0.013}$	28.47 / 40	0.91
z_3	$ggg + gg$	2.80	$2.83^{+0.26}_{-0.36}$	0.622	$0.623^{+0.065}_{-0.073}$	0.3107	$0.3120^{+0.0095}_{-0.011}$	35.36 / 31	0.27
	$ggg + g\kappa$	2.31	$2.37^{+0.17}_{-0.23}$	0.742	0.735 ± 0.038	0.278	$0.290^{+0.025}_{-0.038}$	25.87 / 31	0.73
	$gg + g\kappa$	2.32	$2.33^{+0.11}_{-0.14}$	0.750	0.747 ± 0.039	0.3050	$0.3057^{+0.0091}_{-0.010}$	26.88 / 37	0.89
	$ggg + gg + g\kappa$	2.43	$2.44^{+0.11}_{-0.13}$	0.719	0.718 ± 0.034	0.3146	$0.3156^{+0.0095}_{-0.011}$	47.63 / 51	0.61
z_4	$ggg + gg$	2.54	$2.57^{+0.27}_{-0.41}$	0.707	$0.714^{+0.091}_{-0.10}$	0.3003	$0.3015^{+0.0086}_{-0.0097}$	48.57 / 36	0.08
	$ggg + g\kappa$	2.41	$2.45^{+0.17}_{-0.21}$	0.746	0.744 ± 0.033	0.296	$0.307^{+0.026}_{-0.038}$	31.86 / 36	0.67
	$gg + g\kappa$	2.390	$2.403^{+0.099}_{-0.12}$	0.750	0.748 ± 0.033	0.2934	$0.2942^{+0.0085}_{-0.0094}$	37.37 / 43	0.71
	$ggg + gg + g\kappa$	2.411	$2.423^{+0.096}_{-0.11}$	0.746	0.744 ± 0.031	0.3012	$0.3020^{+0.0086}_{-0.0097}$	58.6 / 59	0.49

Table 4

Parameter best-fit (BF) values and marginalised constraints for each of the probe combinations in all 4 redshift bins. The errors quoted correspond to 68% confidence level intervals; both upper and lower bounds are specified when the posterior distribution is non-Gaussian. We also quote the chi-square statistics χ^2 (along with the corresponding number of degrees of freedom N_{dof} for comparison), as well as the associated probability-to-exceed (PTE) of the theoretical prediction corresponding to the best-fit values.

parameters are deterministically related to the linear bias b_1 . Nevertheless, some interesting insights can be gained from these results.

First, focusing on the Ω_m constraints, we can see that its derived value is determined by the shape of the galaxy auto-correlation, as its value and statistical uncertainties are consistent across all data combinations including C_ℓ^{gg} . The combination $\Phi_{LL\ell}^{ggg} + C_\ell^{g\kappa}$, in turn, yields uncertainties that are approximately 3 times larger, although the recovered constraints on Ω_m are consistent, well within 1σ , with those found by other data combinations across most redshift bins. The exception in this case is z_2 , where this data combination recovers a value of Ω_m that is in $\sim 2\sigma$ tension with that preferred by the datasets including C_ℓ^{gg} , as well as with the value measured by *Planck* (Planck Collaboration et al. 2020a). This tension is also apparent in the two-dimensional contours of Fig. 6. Interestingly, this is the only redshift bin in which one of the model parameters (Ω_m) hits the prior, showing that this data combination is particularly insensitive to this parameter. The preference for a higher Ω_m in this case may be a statistical fluctuation, or it may be caused by some of our simplifying assumptions. We will explore this further in future work.

Secondly, we find that, in most cases, all probe combinations are able to obtain constraints on σ_8 that are consistent within $\sim 1\sigma$. Interestingly, we find that all combinations that include the galaxy- κ cross-correlation obtain significantly tighter constraints, in remarkable agreement with each other. $C_\ell^{g\kappa}$ is thus vital when measuring σ_8 , and the agreement between different

data combinations is a direct consequence of the compatibility between the galaxy two-point and three-point correlators within the model used here. As we anticipated in the previous section, although the constraints from the $C_\ell^{gg} + \Phi_{LL\ell}^{ggg}$ are less precise than other combinations, it is reassuring to see that we are able to obtain constraints on σ_8 in the absence of lensing information that are largely in agreement with the other probes. Furthermore, the constraints found in the (Ω_m, σ_8) plane are almost orthogonal under this data combination. It is interesting to note that the $gg + ggg$ combination seems to favour consistently lower values of σ_8 across all redshift bins. This is particularly evident in the first redshift bin, displaying a $\sim 2\sigma$ tension between this data combination and the 2×2 -point dataset and, to a lesser extent in the third redshift bin, which recovers a $\sim 1.5\sigma$ downwards shift. As we discussed in Section 4.2.2, and further explored in Appendix A, the constraints on σ_8 found from this data combination are critically dependent on our assumptions regarding the relationship between the different bias parameters. Thus, the preference for a lower σ_8 could be a result of the coevolution relations we have adopted here. In addition to enabling these valuable consistency tests, the inclusion of the galaxy bispectrum in addition to the traditional 2×2 -point data combination leads to a $\sim 10\%$ improvement in the constraint on σ_8 . We note that, regardless of which data combination is used, the values of σ_8 we recover are systematically low with respect to that preferred by *Planck*.

This fact is evident in the upper panel of Fig. 7. The figure shows the constraints on the amplitude of matter fluctuations

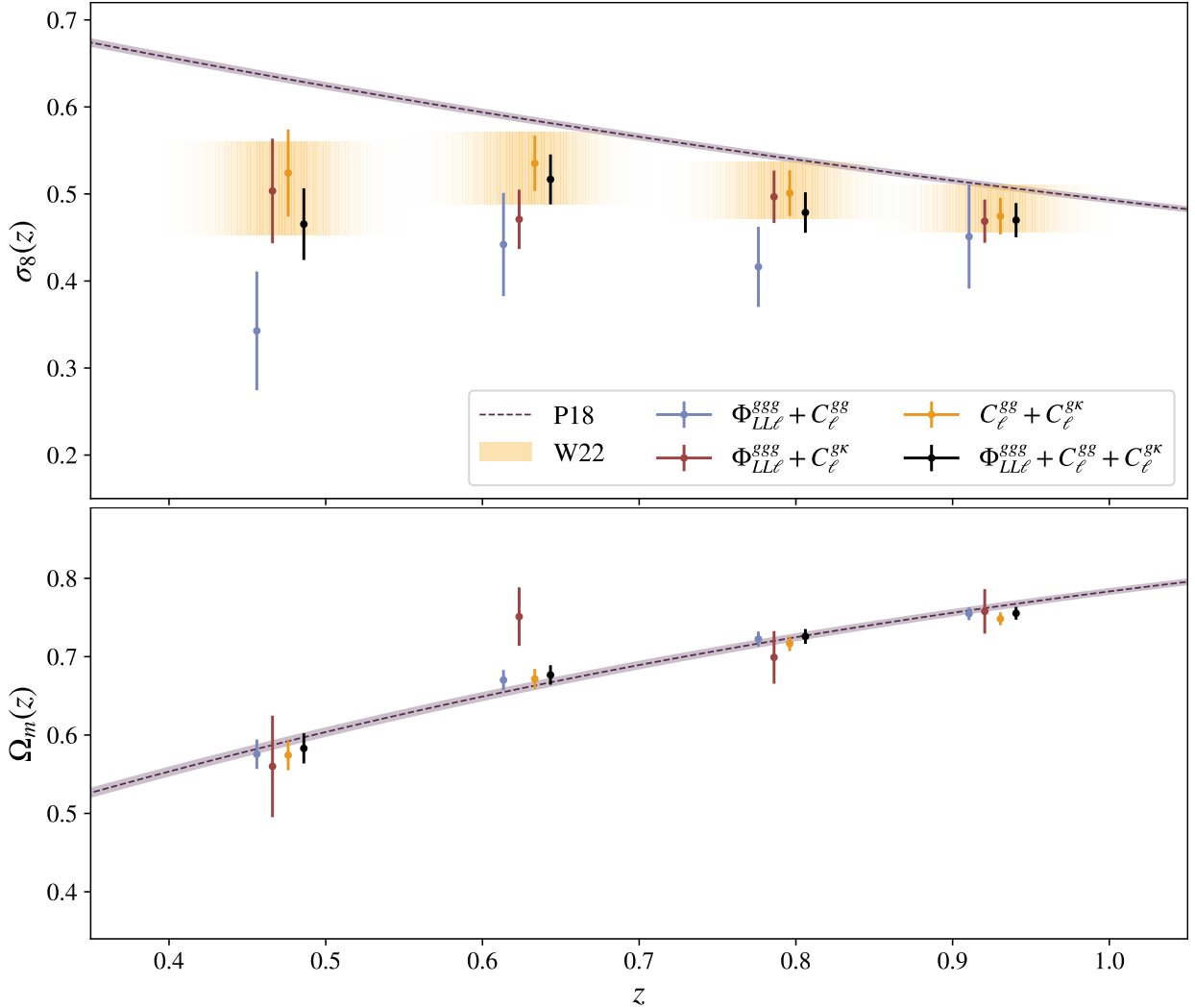


Figure 7. Top panel: σ_8 constraints as a function of redshift, constructed from Eq. 50. We show constraints from all four probe combinations shown in Fig. 6. For comparison, we also include early-universe constraints on σ_8 presented in Planck Collaboration et al. (2020a) – P18 on the figure – as well as CMB lensing tomography constraints from White et al. (2022) – shortened to W22 above – which were derived from the traditional power spectrum combination $C_\ell^{gg} + C_\ell^{g\kappa}$. The W22 constraints were obtained from identical data as used in this work, but with slightly different modelling choices and scale cuts. Bottom panel: Ω_m constraints as a function of redshift, constructed from Eq. 51. Similarly, this figure shows the constraints on Ω_m for each probe combination using the same colour scheme. We also show *Planck* constraints as the dashed purple line.

$\sigma_8(z)$ at the mean redshift of each of the samples studied here. The time-dependent amplitude is defined as

$$\sigma_8(z) \equiv \sigma_8 D(z|\Omega_m), \quad (50)$$

where $D(z|\Omega_m)$ is the linear growth factor at redshift z , implicitly dependent on Ω_m , and normalised so that $D(0|\Omega_m) = 1$. The figure shows the constraints found from the same data combinations discussed above, in addition to the best-fit prediction from *Planck* (purple dashed line). We find values of $\sigma_8(z)$ that are consistently lower than the *Planck* prediction. Qualitatively, this result was also reported in White et al. (2022). The constraints on $\sigma_8(z)$ found there, shown in Fig. 7 as yellow bands are largely in agreement with our 2×2 -point constraints, in spite of the significant differences in the modelling choices used here (e.g. tree-level bias parametrisation in Eulerian space, different scale cuts, shot noise marginalisation). Our results are also in rough agreement with those found by Sailer et al. (2025b). The evidence for a lower σ_8 is stronger in the first bin, as was also found in these works. We also provide an equivalent figure for the evolution of Ω_m with redshift

(lower panel of Fig. 50). We generate the time-dependent non-relativistic matter fraction using

$$\Omega_m(z) = \frac{\Omega_m(1+z)^3}{\Omega_m(1+z)^3 + (1-\Omega_m)}. \quad (51)$$

One data point stands out – the $ggg + g\kappa$ constraint in z_2 , as mentioned earlier – but all other constraints points are in very good agreement with early-universe constraints from *Planck*, shown by the purple dashed line. It is worth noting that, as discussed above, these constraints are driven by the shape of the large-scale matter power spectrum, which is most tightly constrained by the C_ℓ^{gg} measurements. Given the relative simplicity of the model used here, we refrain from quantifying or interpreting the level of tension between these results and the CMB predictions. This will be addressed in upcoming work employing a more robust modelling to describe the 2-point and 3-point clustering of galaxies (Verdiani et al. 2025). Nevertheless, we find that all data combinations recover compatible constraints, which indicates that any potential tension is likely not dominated by systematics in any individual measurement.

5. DISCUSSION

This paper presents an attempt at using the projected bispectrum in tandem with the traditional angular power spectrum to conduct a joint cosmological analysis of CMB lensing and galaxy data. To do so, we measure the “filtered-squared bispectrum” (FSB) estimator as a proxy for the projected bispectrum. We develop in this paper a self-consistent framework for the generalisation of the FSB, first introduced in H25, to cross-correlations. The FSB estimator is robust to incomplete sky observations and comes with a fully analytical, model-independent covariance which can be efficiently estimated from the data. Theoretical predictions for the FSB estimator can also be built in a straightforward manner from perturbation theory, making the FSB a truly attractive higher-order statistic.

We use data from four photometric DESI Luminous Red Galaxy samples, described in Zhou et al. (2023b) and White et al. (2022), and the CMB lensing convergence map obtained from Planck (Planck Collaboration et al. 2020a) to measure auto- and cross-FSBs. One of our primary results is the detection of both the galaxy bispectrum (ggg) at very high significance ($> 30\sigma$) in all redshift bins, and the galaxy-galaxy-convergence bispectrum ($gg\kappa$) at lower significance ($> 5\sigma$) in three out of the four galaxy samples used in this work. The latter being detected at a low signal-to-noise means that we are not able to use $gg\kappa$ in the second part of the paper, where we conduct a rudimentary cosmological analysis.

In this first cosmological analysis including the projected bispectrum, we simply focus on three parameters – the clustering amplitude σ_8 , the non-relativistic matter fraction Ω_m , and the linear bias b_1 – while keeping other parameters fixed. We identify two new probe combinations that break degeneracies between σ_8 and b_1 : combining the ggg FSB measurements with any of the power spectra (gg or $g\kappa$) allows us to derive complementary constraints on σ_8 and Ω_m , and to test the robustness of the constraints obtained from the standard 2×2 -point combination against observational and modelling systematics. The new $ggg + gg$ combination is especially exciting, potentially yielding a fully local measurement of σ_8 without resorting to using CMB lensing data to break the σ_8 -bias degeneracy.

The addition of the ggg bispectrum to both power spectra ($ggg + gg + g\kappa$ combination) leads to a modest improvement of $\sim 10\%$ on the σ_8 constraints. Further improvement may be achievable with more sensitive datasets, allowing us to use the $gg\kappa$ bispectrum, or pushing to scales smaller than the conservative cuts assumed here. We also find that the $g\kappa$ cross-spectrum is indispensable to obtain tight constraints on σ_8 (and similarly with the gg auto-spectrum for Ω_m). All combinations studied yield consistent results: $gg + g\kappa$ and $ggg + g\kappa$ are consistent between themselves at the 1σ level in σ_8 , and at the 2σ level with $ggg + gg$. All combinations give σ_8 values consistently lower than inferred from Planck measurements, in agreement with previous CMB lensing tomography studies conducted on the same data (White et al. 2022, using the standard $gg + g\kappa$ combination with a different modelling approach). In particular, we find that the $ggg + gg$ combination favours even lower σ_8 values than other probe combinations at low redshift. We argue, however, that this result is highly dependent on some of our analysis choices, and thus refrain from fully interpreting this result in terms of a cosmological tension.

Indeed, our modelling of the bispectrum comes with various

caveats: in this first approach, we only model the bispectrum at the tree-level (a decision which we must compensate for by implementing conservative scale cuts) and, critically, choose to use empirical coevolution relations to express higher-order bias parameters (b_2 and b_s). These coevolution relations play an important role in our final results, as they essentially dictate the effective scaling of the bispectrum with b_1 – and thus, how efficiently it can break parameter degeneracies when combined with power spectrum measurements. Upcoming work (Verdiani et al. 2025) will focus on providing a better model for the bispectrum, in combination with a modelling of the power spectrum at the 1-loop level. This will allow us to push to smaller scales and to constrain the higher-order bias parameters directly from the data, without having to resort to using coevolution relations. In this scenario, the bispectrum is a critical tool to improve the constraints on b_2 and b_s , potentially leading to a relatively larger improvement on the final cosmological constraints obtained from power spectra than we report here. Eventually, the use of hybrid approaches to model galaxy bias (e.g. Modi et al. 2020; Hadzhiyska et al. 2021) will be required to extend the range of scales over which the bispectrum may be used for cosmological inference.

In summary, we have included for the first time the projected bispectrum in a tomographic cosmological analysis of galaxy clustering and CMB lensing. Despite our simplistic bispectrum model and conservative scale cuts, we have shown that the projected bispectrum is able to provide consistent and improved cosmological constraints when combined with power spectrum measurements. This work illustrates the potential of the projected bispectrum as a cosmological probe, and provides a first tentative blueprint for its implementation into inference pipelines using the FSB estimator.

ACKNOWLEDGMENTS

We would like to thank Sergi Novell-Masot, Emiliano Sefusatti, Francesco Verdiani, and Matteo Zennaro for useful comments and discussions. LH is supported by a Hintze studentship, which is funded through the Hintze Family Charitable Foundation. DA acknowledges support from STFC and the Beecroft Trust. We made extensive use of computational resources at the University of Oxford Department of Physics, funded by the John Fell Oxford University Press Research Fund. AN acknowledges support from the European Research Council (ERC) under the European Union’s Horizon 2020 research and innovation program with Grant agreement No. 101163128.

REFERENCES

- Alonso D., Sanchez J., Slosar A., LSST Dark Energy Science Collaboration 2019, *MNRAS*, 484, 4127
- Alonso D., Fabbian G., Storey-Fisher K., Eilers A.-C., García-García C., Hogg D. W., Rix H.-W., 2023, *J. Cosmology Astropart. Phys.*, 2023, 043
- Barreira A., Lazeyras T., Schmidt F., 2021, *J. Cosmology Astropart. Phys.*, 2021, 029
- Bartelmann M., Schneider P., 2001, *Phys. Rep.*, 340, 291
- Bernardeau F., Colombi S., Gaztañaga E., Scoccimarro R., 2002, *Phys. Rep.*, 367, 1
- Biagetti M., Castiblanco L., Noreña J., Sefusatti E., 2022, *J. Cosmology Astropart. Phys.*, 2022, 009
- Burger P. A., et al., 2024, *A&A*, 683, A103
- Cagliari M. S., Barberi-Squarotti M., Pardede K., Castorina E., D’Amico G., 2025, *arXiv e-prints*, p. arXiv:2502.14758
- Calabrese E., Smidt J., Amblard A., Cooray A., Melchiorri A., Serra P., Heavens A., Munshi D., 2010, *Phys. Rev. D*, 81, 043529
- Carlstrom J. E., Holder G. P., Reese E. D., 2002, *ARA&A*, 40, 643
- Chisari N. E., Alonso D., Krause E., Leonard C. D., et al., 2019, *ApJS*, 242, 2

- Cooray A., 2001, *Phys. Rev. D*, 64, 043516
- Cooray A., Hu W., 2001, *ApJ*, 548, 7
- Cowell J. A., Alonso D., Liu J., 2024, *MNRAS*, 535, 3129
- Desjacques V., Jeong D., Schmidt F., 2018, *Phys. Rep.*, 733, 1
- Dey A., et al., 2019, *AJ*, 157, 168
- Eickenberg M., et al., 2022, *arXiv e-prints*, p. arXiv:2204.07646
- Farren G. S., Sherwin B. D., Bolliet B., Namikawa T., Ferraro S., Krolewski A., 2023, *arXiv e-prints*, p. arXiv:2311.04213
- Farren G. S., et al., 2024, *ApJ*, 966, 157
- Farren G. S., et al., 2025, *Phys. Rev. D*, 111, 083516
- Foreman-Mackey D., Hogg D. W., Lang D., Goodman J., 2013, *PASP*, 125, 306
- Friedrich O., et al., 2018, *Phys. Rev. D*, 98, 023508
- Fry J. N., Gaztanaga E., 1993, *ApJ*, 413, 447
- García-García C., Alonso D., Bellini E., 2019, *J. Cosmology Astropart. Phys.*, 2019, 043
- Gatti M., et al., 2022, *Phys. Rev. D*, 106, 083509
- Górski K. M., Hivon E., Banday A. J., Wandelt B. D., Hansen F. K., Reinecke M., Bartelmann M., 2005, *ApJ*, 622, 759
- Grewal N., Zuntz J., Tröster T., Amon A., 2022, *The Open Journal of Astrophysics*, 5, 13
- Hadzhiyska B., García-García C., Alonso D., Nicola A., Slosar A., 2021, *Journal of Cosmology and Astroparticle Physics*, 2021, 020
- Harscouet L., Cowell J. A., Ereira J., Alonso D., Camacho H., Nicola A., Slosar A., 2025, *The Open Journal of Astrophysics*, 8, 6
- Ivanov M. M., Philcox O. H. E., Nishimichi T., Simonović M., Takada M., Zaldarriaga M., 2022, *Phys. Rev. D*, 105, 063512
- Jasche J., Wandelt B. D., 2013, *MNRAS*, 432, 894
- Kim J., et al., 2024, *J. Cosmology Astropart. Phys.*, 2024, 022
- Krolewski A., Ferraro S., White M., 2021, *J. Cosmology Astropart. Phys.*, 2021, 028
- Lavaux G., Jasche J., Leclercq F., 2019, *arXiv e-prints*, p. arXiv:1909.06396
- Lazeyras T., Schmidt F., 2018, *J. Cosmology Astropart. Phys.*, 2018, 008
- Lazeyras T., Wagner C., Baldauf T., Schmidt F., 2016, *J. Cosmology Astropart. Phys.*, 2016, 018
- Lewis A., Challinor A., 2006, *Phys. Rep.*, 429, 1
- Li Y., Singh S., Yu B., Feng Y., Seljak U., 2019, *J. Cosmology Astropart. Phys.*, 2019, 016
- Limber D. N., 1953, *ApJ*, 117, 134
- LoVerde M., Afshordi N., 2008, *Phys. Rev. D*, 78, 123506
- Madhavacheril M. S., et al., 2024, *ApJ*, 962, 113
- Mandelbaum R., 2018, *ARA&A*, 56, 393
- Massara E., et al., 2023, *ApJ*, 951, 70
- McDonald P., Roy A., 2009, *J. Cosmology Astropart. Phys.*, 2009, 020
- Modi C., Chen S.-F., White M., 2020, *Monthly Notices of the Royal Astronomical Society*, 492, 5754
- Montandon T., Adamek J., Hahn O., Noreña J., Rampf C., Stahl C., van Tent B., 2023, *Journal of Cosmology and Astroparticle Physics*, 2023, 043
- Moradinezhad Dizgah A., Lee H., Schmittfull M., Dvorkin C., 2020, *J. Cosmology Astropart. Phys.*, 2020, 011
- Munshi D., Namikawa T., Kitching T. D., McEwen J. D., Takahashi R., Bouchet F. R., Taruya A., Bose B., 2020a, *MNRAS*, 493, 3985
- Munshi D., Namikawa T., Kitching T. D., McEwen J. D., Bouchet F. R., 2020b, *MNRAS*, 498, 6057
- Nicola A., et al., 2020, *J. Cosmology Astropart. Phys.*, 2020, 044
- Obreschkow D., Power C., Bruderer M., Bonvin C., 2013, *ApJ*, 762, 115
- Oliveira Franco F., Hadzhiyska B., Alonso D., 2022, *arXiv e-prints*, p. arXiv:2206.11005
- Peebles P. J. E., 1980, *The large-scale structure of the universe*. Princeton University Press
- Philcox O. H. E., 2021, *Phys. Rev. D*, 104, 123529
- Philcox O. H. E., Flöss T., 2024, *arXiv e-prints*, p. arXiv:2404.07249
- Planck Collaboration et al., 2020a, *A&A*, 641, A6
- Planck Collaboration et al., 2020b, *A&A*, 641, A8
- Porqueres N., Heavens A., Mortlock D., Lavaux G., 2022, *MNRAS*, 509, 3194
- Porqueres N., Heavens A., Mortlock D., Lavaux G., Makinen T. L., 2023, *arXiv e-prints*, p. arXiv:2304.04785
- Porth L., Heydenreich S., Burger P., Linke L., Schneider P., 2024, *A&A*, 689, A227
- Qu F. J., et al., 2025, *Phys. Rev. D*, 111, 103503
- Régalo-Saint Blancard B., et al., 2024, *Phys. Rev. D*, 109, 083535
- Sailer N., DeRose J., Ferraro S., Chen S.-F., Zhou R., White M., Kim J., Madhavacheril M., 2025a, *Phys. Rev. D*, 111, 103540
- Sailer N., et al., 2025b, *J. Cosmology Astropart. Phys.*, 2025, 008
- Schmittfull M., Baldauf T., Seljak U., 2015, *Phys. Rev. D*, 91, 043530
- Scoccimarro R., 2015, *Physical Review D*, 92, 083532
- Scoccimarro R., Couchman H. M. P., Frieman J. A., 1999, *ApJ*, 517, 531
- Secco L. F., et al., 2022, *Phys. Rev. D*, 105, 103537
- Simpson F., James J. B., Heavens A. F., Heymans C., 2011, *Phys. Rev. Lett.*, 107, 271301
- Smidt J., Amblard A., Byrnes C. T., Cooray A., Heavens A., Munshi D., 2010, *Phys. Rev. D*, 81, 123007
- Sugiyama N. S., Saito S., Beutler F., Seo H.-J., 2019, *Monthly Notices of the Royal Astronomical Society*, 484, 364
- Takada M., Jain B., 2004, *MNRAS*, 348, 897
- Takahashi R., Nishimichi T., Namikawa T., Taruya A., Kayo I., Osato K., Kobayashi Y., Shirasaki M., 2020, *ApJ*, 895, 113
- Vakili M., et al., 2023, *A&A*, 675, A202
- Verdiani F., Harscouet L., Zennaro M., Alonso D., Hadzhiyska B., 2025, *arXiv e-prints*, p. arXiv:2510.17796
- White M., et al., 2022, *J. Cosmology Astropart. Phys.*, 2022, 007
- Xu H., et al., 2023, *Science China Physics, Mechanics, and Astronomy*, 66, 129811
- Yip J. H. T., Biagetti M., Cole A., Viswanathan K., Shiu G., 2024, *J. Cosmology Astropart. Phys.*, 2024, 034
- Zhou R., et al., 2023a, *AJ*, 165, 58
- Zhou R., et al., 2023b, *J. Cosmology Astropart. Phys.*, 2023, 097
- de Belsunce R., et al., 2025, *arXiv e-prints*, p. arXiv:2506.22416

APPENDIX

A. EFFECT OF USING COEVOLUTION RELATIONS

Throughout this paper, we use coevolution relations of bias parameters to simplify our inference pipeline and redirect the constraining power of the FSB probes towards parameters of cosmological interest. For completeness, we repeat their expressions here (Lazeyras et al. 2016; Lazeyras & Schmidt 2018):

$$b_2(b_1) = 0.412 - 2.143b_1 + 0.929b_1^2 + 0.008b_1^3, \quad (\text{A1})$$

$$b_s(b_1) = -\frac{2}{7}(b_1 - 1). \quad (\text{A2})$$

In this appendix we explore how these coevolution relations affect our analysis. We show this by comparing different approaches to modelling the bispectrum. Note that here, for simplicity and ease of interpretation, we will fix Ω_m to its fiducial value (see Table 1), and only vary σ_8 and the bias parameters.

The first approach was to simply set both of the b_2 and b_s parameters to zero, effectively making the corresponding terms in the tree-level bispectrum (Eqs. 29 and 30) vanish. Fig. 8 shows the difference in the parameter contours resulting from this choice with respect to the results obtained assuming coevolution relations to determine b_2 and b_s . The effect is particularly significant in the case of the $\Phi_{LLL}^{ggg} + C_\ell^{gg}$ probe combination, for which setting $b_2 = b_s = 0$ leads to a significant shift in the contours along the C_ℓ^{gg} degeneracy direction (shown as the grey contours of the first panel in Fig. 8). Using coevolution relations pushes the

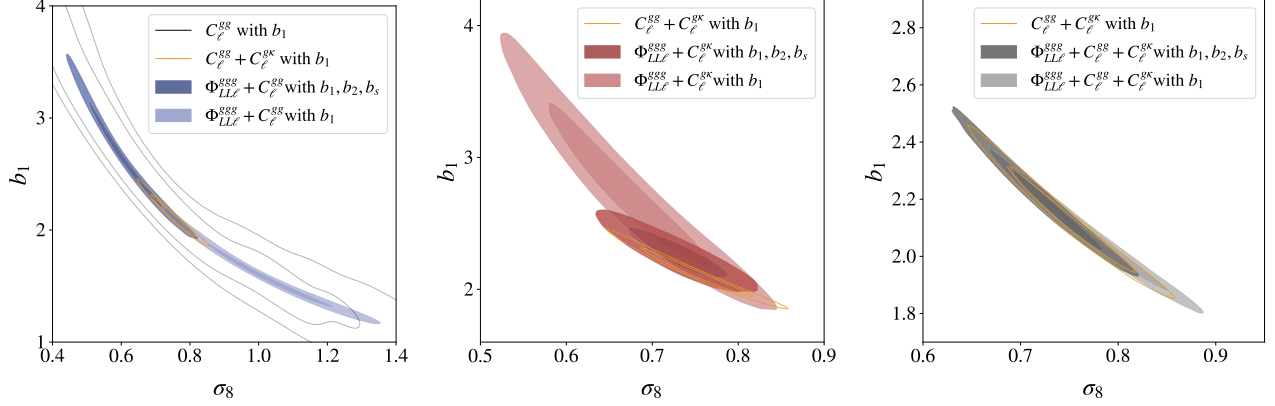


Figure 8. Plots showing the effect of using b_1 , b_2 and b_s while fixing the latter two using coevolution relations (dark contours), and that of using b_1 only in the bispectrum analysis (i.e. setting $b_2 = b_s = 0$, shown by the lighter contours). The yellow contours show for comparison the power-spectra-only constraints, which are unaffected by this test as they only depend on the linear bias in this analysis (thus the yellow contours remain the same in all three panels). These contours were generated for the galaxy data in the second redshift bin, z_2 .

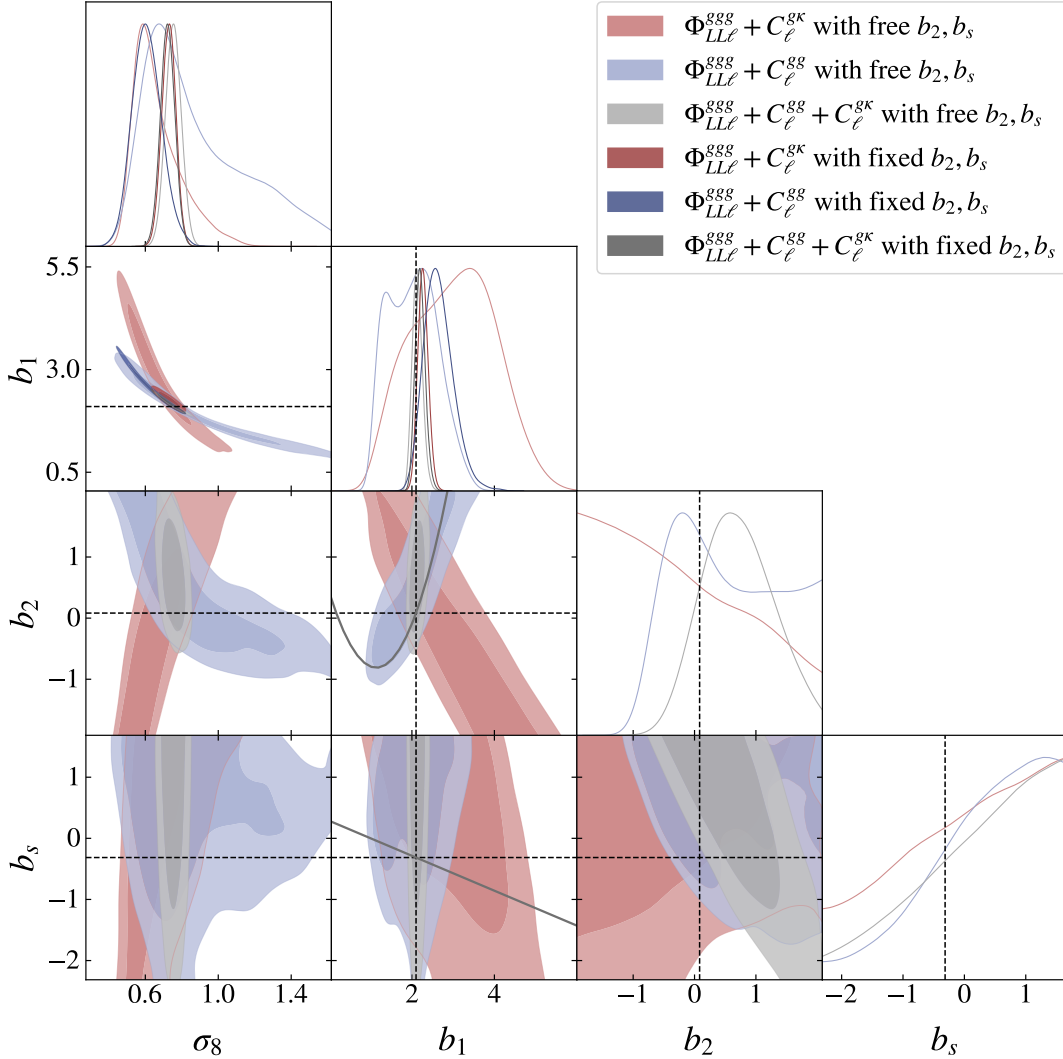


Figure 9. Plot showing constraints obtained when freeing the b_2 and b_s parameters (light contours) as opposed to fixing them using coevolution relations (darker contours in the $b_1 - \sigma_8$ block). We show the coevolution relations (Eqs. A1 and A2) as dark grey lines in the $b_2 - b_1$ and $b_s - b_1$ blocks. The black dashed lines along the b_2 and b_s rows and columns show the values of those parameters obtained via coevolution, for the published value of the linear bias for this redshift bin (z_2) – we use those as central values for the uniform priors placed on b_2 and b_s . We only show the area of parameter space allowed by the priors.

constraints towards lower values of σ_8 (and higher b_1 values, as discussed in Section 4.2.2). The combination containing all probes similarly gets pushed towards higher σ_8 values, although the effect is less extreme (as the constraints are dominated by the power spectra, which are insensitive to b_2 and b_s at the tree level). The addition of the quadratic and tidal biases via coevolution significantly shrinks the contours for the $\Phi_{LL\ell}^{ggg} + C_\ell^{g\kappa}$ probe combination, pushing it closer to the power-spectra contour (this time towards slightly higher σ_8 values, and much lower bias).

We also explore the impact of allowing b_2 and b_s to vary freely, instead of fixing them to b_1 via coevolution relations. The priors defined for these two parameters still make use of the coevolution relations, but allow a wider range of bias values: we use $\mathcal{U}[b_2(b_1) - 2, b_2(b_1) + 2]$ and $\mathcal{U}[b_s(b_1) - 2, b_s(b_1) + 2]$ as priors for b_2 and b_s respectively, where b_1 here is the published linear bias value in the redshift bin (see Table 2), taken from White et al. (2022). Interestingly, as can be seen by comparing the light blue and light red contours in both Fig. 8 and Fig. 9, the constraints obtained in this approach are similar to those obtained when setting the non-linear biases to zero. In general, the ggg FSB does not have enough constraining power on its own to fully constrain b_1 , b_2 and b_s simultaneously, as shown by the light blue, red or gray contours for the non-linear bias parameters in Fig. 9, which are largely unconstrained. In order to self-consistently constrain higher-order bias parameters from the power- and bispectrum, it will thus be crucial to push the analysis to smaller scales by modelling the power spectrum up to 1-loop and potentially moving beyond tree-level bispectra. We leave this analysis for future work.

The coevolution relations thus play an important role in the final σ_8 constraints recovered from the galaxy-only probes, and for the final b_1 constraints obtained from the $\Phi_{LL\ell}^{ggg} + C_\ell^{g\kappa}$ combination. The object of future work will be to test thoroughly these coevolution relations over a large range of galaxy samples.

B. STOCHASTIC CONTRIBUTIONS

In this appendix we derive the expressions for the noise contributions to the $gg\kappa$ bispectrum, Eq. 32. In Appendix D of H25, we derived the equivalent term for the ggg bispectrum (Eq. 31), in which case all fields measured receive a shot-noise contribution due to the discreteness of the tracer. Here, that is not the case for the third field (the CMB convergence κ). Let us see what this implies for the additional shot noise terms contributing to the $gg\kappa$ bispectrum.

Observationally, we estimate the FSB from pixelised maps of the galaxy overdensity $\delta_p = \frac{N_p}{\bar{N}} - 1$, where N_p denotes the number of galaxies in pixel p , and \bar{N} is the mean number of galaxies per pixel. Assuming galaxies to be Poisson tracers of the underlying density field, the first two moments of the galaxy density field are given by

$$\begin{aligned}\langle N_p \rangle_{\text{Pois}} &= \bar{N}_p = \bar{N}(1 + \delta_p), \\ \langle N_p N_q \rangle_{\text{Pois}} &= \bar{N}_p \bar{N}_q + \delta_{pq}^K \bar{N}_p,\end{aligned}\tag{B1}$$

where δ_{pq}^K denotes the Kronecker delta and we have only performed the Poisson ensemble average (Peebles 1980).

Similarly, we can denote the value of the convergence field at pixel p as K_p . The first moment of the convergence field, is simply $\langle K_p \rangle_{\text{Pois}} = K_p$ as the convergence is not a discretely-sampled field.

Now let us look at cross-moments, which we will need for the upcoming calculations: we have

$$\begin{aligned}\langle N_p K_q \rangle_{\text{Pois}} &= \bar{N}_p K_q \\ \langle N_p N_q K_r \rangle_{\text{Pois}} &= (1 - \delta_{pq}^K) \bar{N}_p \bar{N}_q K_r + \delta_{pq}^K (\bar{N}_p^2 + \bar{N}_p) K_r \\ &= \bar{N}^2 (1 + \delta_p + \delta_q + \delta_p \delta_q) K_r + \delta_{pq}^K \bar{N} (1 + \delta_p) K_r\end{aligned}\tag{B2}$$

With these tools in hand, we can now try to derive the 3-point correlation functions of fields g , g and κ :

$$\begin{aligned}\langle gg\kappa \rangle_{\text{Pois}}|_{\text{pix}=p,q,r} &\equiv \left\langle \left(\frac{N_p - \bar{N}}{\bar{N}} \right) \left(\frac{N_q - \bar{N}}{\bar{N}} \right) K_r \right\rangle \\ &= \frac{1}{\bar{N}^2} [\langle N_p N_q K_r \rangle - \bar{N} \langle N_q \rangle K_r - \bar{N} \langle N_p \rangle K_r + \bar{N}^2 K_r] \\ &= \frac{1}{\bar{N}^2} [\bar{N}^2 (1 + \delta_p + \delta_q + \delta_p \delta_q) K_r + \delta_{pq}^K \bar{N} (1 + \delta_p) K_r - \bar{N}^2 (1 + \delta_q + \delta_p) K_r] \\ &= \frac{1}{\bar{N}^2} [\bar{N}^2 \delta_p \delta_q K_r + \delta_{pq}^K \bar{N} (1 + \delta_p) K_r]\end{aligned}\tag{B4}$$

Now taking the expectation value over fields g , κ , and assuming $\langle g \rangle$ and $\langle \kappa \rangle$ to be 0 over field realisations, we obtain:

$$\langle gg\kappa \rangle = \frac{1}{\bar{N}^2} \langle (N_p - \bar{N})(N_q - \bar{N}) K_r \rangle = \langle \delta_p \delta_q \kappa_r \rangle + \delta_{pq}^K \frac{1}{\bar{N}} \langle \delta_p \kappa_r \rangle\tag{B5}$$

We now can express Eq. B5 in harmonic space, thus obtaining the corresponding projected bispectrum:

$$\begin{aligned} \langle g_{\ell m} g_{\ell' m'} \kappa_{\ell'' m''} \rangle &= \sum_{p,q,r} \Omega_{\text{pix}}^3 \left(\langle \delta_p \delta_q \kappa_r \rangle + \delta_{pq}^{\mathcal{K}} \frac{1}{N} \langle \delta_p \kappa_r \rangle \right) Y_{\ell m p}^* Y_{\ell' m' q}^* Y_{\ell'' m'' r}^* \\ &= \Omega_{\text{pix}}^3 \sum_{p,q,r} \langle \delta_p \delta_q \kappa_r \rangle Y_{\ell m p}^* Y_{\ell' m' q}^* Y_{\ell'' m'' r}^* + \frac{\Omega_{\text{pix}}^3}{N} \sum_{p,r} \langle \delta_p \kappa_r \rangle Y_{\ell m p}^* Y_{\ell' m' p}^* Y_{\ell'' m'' r}^* \end{aligned} \quad (\text{B6})$$

where we have used the shorthand $Y_{\ell m p} \equiv Y_{\ell m}(\hat{\mathbf{n}}_p)$, and where Ω_{pix} denotes the average pixel area.

Noticing that

$$\langle \delta_i \delta_j \delta_k \rangle = \sum_{(\ell m)_{123}} Y_{\ell_1 m_1 i} Y_{\ell_2 m_2 j} Y_{\ell_3 m_3 k} \mathcal{G}_{m_1 m_2 m_3}^{\ell_1 \ell_2 \ell_3} b_{\ell_1 \ell_2 \ell_3} \quad \text{and} \quad \Omega_{\text{pix}} \sum_i Y_{\ell m i} Y_{\ell' m' i}^* = \delta_{\ell \ell'}^{\mathcal{K}} \delta_{m m'}^{\mathcal{K}}, \quad (\text{B7})$$

we can rewrite the first term in Eq. B6 as

$$(1) \equiv \Omega_{\text{pix}}^3 \sum_{p,q,r} \left(\sum_{(\ell m)_{123}} Y_{\ell_1 m_1 p} Y_{\ell_2 m_2 q} Y_{\ell_3 m_3 r} \mathcal{G}_{m_1 m_2 m_3}^{\ell_1 \ell_2 \ell_3} b_{\ell_1 \ell_2 \ell_3}^{g g \kappa} \right) Y_{\ell m p}^* Y_{\ell' m' q}^* Y_{\ell'' m'' r}^* = \mathcal{G}_{m m' m''}^{\ell \ell' \ell''} b_{\ell \ell' \ell''}^{g g \kappa}, \quad (\text{B8})$$

which simply corresponds to the main projected bispectrum term in the absence of shot noise.

The second term however is introduced due to the stochastic nature of the galaxy density field; if we write the two-point correlation function in the second term of Eq. B6 as

$$\langle \delta_i \delta_j \rangle = \sum_{(\ell m)_{12}} Y_{\ell_1 m_1 i} Y_{\ell_2 m_2 j} \delta_{\ell_1 \ell_2}^{\mathcal{K}} \delta_{m_1 m_2}^{\mathcal{K}} C_{\ell_1}^{\delta \delta} = \sum_{(\ell m)} Y_{\ell m i} Y_{\ell m j} C_{\ell}^{\delta \delta}, \quad (\text{B9})$$

we can simplify the term to:

$$\begin{aligned} (2) &\equiv \frac{\Omega_{\text{pix}}^2}{N} \sum_{p,q} Y_{\ell m p}^* Y_{\ell' m' p}^* Y_{\ell'' m'' q}^* \sum_{(\ell_1 m_1)} Y_{\ell_1 m_1 p} Y_{\ell_1 m_1 q} C_{\ell_1}^{g \kappa} \\ &= \frac{\Omega_{\text{pix}}}{N} C_{\ell''}^{g \kappa} \sum_p Y_{\ell m p}^* Y_{\ell' m' p}^* Y_{\ell'' m'' p} \end{aligned} \quad (\text{B10})$$

We use the property of spherical harmonics' complex conjugates, $Y_{\ell m}^* = (-1)^m Y_{\ell -m}$, to rename our indices: $m \rightarrow -m$ and $m' \rightarrow -m'$. This allows us to recover a term that resembles (discrete) Gaunt coefficients:

$$(2) = \frac{1}{N} C_{\ell''}^{g \kappa} \mathcal{G}_{m m' m''}^{\ell \ell' \ell''}. \quad (\text{B11})$$

Therefore the Poisson contribution for an FSB which is measured on two discretely-sampled fields (here the galaxy overdensity field δ_g) and a continuous one (like the CMB convergence κ), is of the form

$$\Phi_{LLb, \text{stoch}}^{g g \kappa} = \sum_{(\ell)_{123}} h_{\ell_1 \ell_2 \ell_3}^2 K_{\ell_1 \ell_2 \ell_3}^{LLb} \left[\frac{1}{\bar{n}} C_{\ell_3}^{g \kappa} \right] \quad (\text{B12})$$

As this term depends on the cross power spectrum of δ_g and κ , it will scale with bias accordingly. This additional bias dependence could potentially further help break degeneracies between bias parameters and parameters of cosmological interest, like σ_8 .

C. MULTIFIELD COVARIANCE

The aim of this appendix is to provide a comprehensive derivation of the terms that contribute to the full covariance used in this analysis. Our data vector is made up of four different types of probes: the galaxy density FSBs $\Phi_{LLb}^{g g g}$, the galaxy density PCLs $C_b^{g g}$, the galaxy-convergence FSBs $\Phi_{LLb}^{g g \kappa}$, and the galaxy-convergence PCLs $C_b^{g \kappa}$. This new data vector offers new potential combination of probes for which we derive, following the logic of the single-field case, the leading off-diagonal terms – denoted by N_{222} and N_{32} in H25. These two terms contribute respectively to the FSB auto-covariance and to the FSB-PCL cross-covariance, and only within the scales filtered in the FSB estimator.

Their contributions to the corresponding correlation matrix (shown in Fig. 10) amount to $\lesssim 30\%$ in the case of N_{222} , and $\lesssim 10\%$ for N_{32} . These are non-negligible contributions which must be accounted for, as they can lead to significant changes in the distribution of residuals (which follow a near-Gaussian distribution once N_{222} and N_{32} are included, as seen in H25) and in the final parameter constraints. These effects are particularly important in our analysis in Section 4.2: Fig. 4 shows that most, if not all in z_1 , FSB data points correspond to the filtered scales, where N_{222} increases the error on measurement. In fact, we find that including N_{222} to the simple Gaussian estimate can, in addition to widening the constraints, lead to a $\sim 1.5\sigma$ shift in σ_8 in the most extreme cases (the number quoted corresponds to the $C_{\ell}^{g g} + \Phi_{LL\ell}^{g g g}$ in redshift bin z_4 , but the effect is generally not as

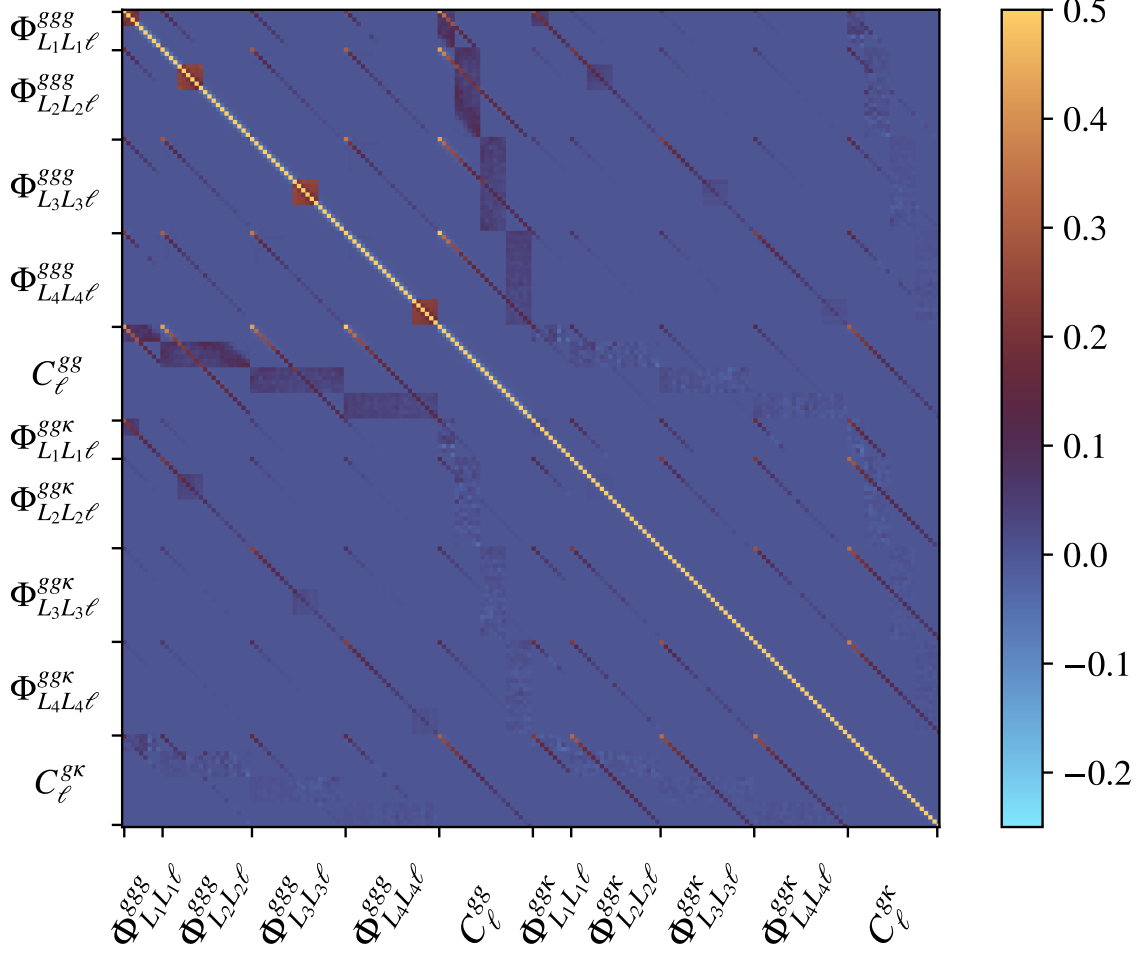


Figure 10. Application of the multi-field covariance derivations presented in this Appendix to the galaxy and convergence data. The example data vector here contains ggg FSB measurements, the gg power spectrum measurement, $gg\kappa$ FSBs, and the $g\kappa$ power spectrum. We plot the correlation matrix (a normalised covariance matrix, where the diagonal is by construction unity) to better highlight off-diagonal contributions – note that we set the maximum value of the colour map to 0.5, as essentially only the main diagonal lies above this threshold. The N_{222} contributions can be seen as small brown or purple squares along the main diagonals in the four large FSB-FSB blocks (although it is barely visible in the $gg\kappa$ - $gg\kappa$ blocks). The N_{32} contributions show up as dark purple bands in the FSB- C_{ℓ} blocks. Due to the weak signal in the generalised $gg\kappa$ and $g\kappa\kappa$ FSBs, this contribution may sometimes appear as a negative contribution (light blue pixels within the N_{32} bands in the $gg\kappa$ - gg , ggg - $g\kappa$ and $gg\kappa$ - $g\kappa$ blocks).

egregious for the full data vector, $C_{\ell}^{gg} + C_{\ell}^{g\kappa} + \Phi_{LL\ell}^{ggg}$). Adding N_{32} to the covariance which already includes N_{222} only leads to minute shifts in the σ_8 contours (a few percent of σ).

We present below the N_{222} and N_{32} derivations for the $\Phi_{LLb}^{ggg} - \Phi_{LLb}^{gg\kappa}$ and $\Phi_{LLb}^{gg\kappa} - \Phi_{LLb}^{g\kappa}$ FSB covariances, as well as for the $\Phi_{LLb}^{ggg} - C_b^{g\kappa}$, $\Phi_{LLb}^{gg\kappa} - C_b^{gg}$, and $\Phi_{LLb}^{gg\kappa} - C_b^{g\kappa}$ FSB-PCL cross covariances.

C.1. FSB covariances

C.1.1. $gg\kappa \times gg\kappa$ covariance

We remind the reader we use the following definition of the FSB in this section:

$$\Phi_{LL\ell}^{gg\kappa} = \frac{1}{(2\ell + 1)} \sum_{m, (\ell m)_{12}} \mathcal{G}_{m_1 m_2 m}^{\ell_1 \ell_2 \ell} W_{\ell_1}^L W_{\ell_2}^L \langle g_{\ell_1 m_1} g_{\ell_2 m_2} \kappa_{\ell m} \rangle, \quad (C1)$$

and that the covariance of random variables X and Y is given by

$$\text{Cov}(X, Y) \equiv \langle XY \rangle - \langle X \rangle \langle Y \rangle \quad (C2)$$

where $\langle XY \rangle$ is the main term and $\langle X \rangle \langle Y \rangle$ the counter-term. From this definition we obtain a 6 point correlation function as the main term, which we will break down into smaller contributions in order to generate analytical predictions for leading-order

terms:

$$\begin{aligned} \langle \hat{\Phi}_{LL}^{ggk} \hat{\Phi}_{L'L'}^{ggk} \rangle &= \frac{1}{(2\ell+1)(2\ell'+1)} \sum_{\ell_{1,2}, \ell'_{1,2}} W_{\ell_1}^L W_{\ell_2}^L W_{\ell'_1}^{L'} W_{\ell'_2}^{L'} \\ &\times \sum_{m, m', m_{1,2}, m'_{1,2}} \mathcal{G}_{-m, m_1, m_2}^{\ell, \ell_1, \ell_2} \mathcal{G}_{-m', m'_1, m'_2}^{\ell', \ell'_1, \ell'_2} \langle g_{\ell_1 m_1} g_{\ell_2 m_2} {}^{\mathcal{K}}_{\ell-m} g_{\ell'_1 m'_1} g_{\ell'_2 m'_2} {}^{\mathcal{K}}_{\ell'-m'} \rangle \end{aligned} \quad (C3)$$

We take a look at the “2 + 2 + 2” decomposition since we know from the single-field case (see Appendix C.1 of H25) that it should give rise to additional contributions along the main diagonal. To keep track of individual combinations of the 6 fields involved in this covariance, we write

$$\langle g_{\ell_1 m_1} g_{\ell_2 m_2} {}^{\mathcal{K}}_{\ell-m} g_{\ell'_1 m'_1} g_{\ell'_2 m'_2} {}^{\mathcal{K}}_{\ell'-m'} \rangle \equiv \langle abcdef \rangle.$$

There are 15 combinations of these 6 fields into pairs:

$$\begin{aligned} \langle abcdef \rangle_{222} &= \langle ab \rangle \langle cd \rangle \langle ef \rangle + \langle ab \rangle \langle ee \rangle \langle df \rangle + \langle ab \rangle \langle cf \rangle \langle de \rangle + \\ &\langle ac \rangle \langle bd \rangle \langle ef \rangle + \langle ac \rangle \langle be \rangle \langle df \rangle + \langle ac \rangle \langle bf \rangle \langle de \rangle + \\ &\langle ad \rangle \langle be \rangle \langle ef \rangle + \langle ad \rangle \langle be \rangle \langle cf \rangle + \langle ad \rangle \langle bf \rangle \langle ce \rangle + \\ &\langle ae \rangle \langle be \rangle \langle df \rangle + \langle ae \rangle \langle bd \rangle \langle cf \rangle + \langle ae \rangle \langle bf \rangle \langle cd \rangle + \\ &\langle af \rangle \langle be \rangle \langle de \rangle + \langle af \rangle \langle bd \rangle \langle ce \rangle + \langle af \rangle \langle be \rangle \langle cd \rangle \end{aligned} \quad (C4)$$

Some vanish due to the closed triangle condition enforced by the bispectrum definition. The remaining terms can be split into 2 groups, noticing that swapping $a \leftrightarrow b$ or $d \leftrightarrow e$ (corresponding to galaxy density fields filtered on scales L and L' respectively) or $c \leftrightarrow f$ (corresponding to convergence fields) does not change the expression. Because the two FSBs might have two different filters however, $a, b \leftrightarrow d, e$ is not equivalent (yet). This gives us 2 groups:

$$\begin{aligned} D_{222} &= \langle ad \rangle \langle be \rangle \langle cf \rangle + \langle ae \rangle \langle bd \rangle \langle cf \rangle \\ &= 2 \left(\delta_{\ell_1 \ell'_1}^{\mathcal{K}} W_{\ell_1}^L W_{\ell'_1}^{L'} C_{\ell_1}^g \times \delta_{\ell_2 \ell'_2}^{\mathcal{K}} W_{\ell_2}^L W_{\ell'_2}^{L'} C_{\ell_2}^g \times \delta_{\ell \ell'}^{\mathcal{K}} C_{\ell}^g \right) \end{aligned} \quad (C5)$$

and

$$\begin{aligned} N_{222} &= \langle ad \rangle \langle bf \rangle \langle ce \rangle + \langle af \rangle \langle bd \rangle \langle ce \rangle + \langle ae \rangle \langle bf \rangle \langle cd \rangle + \langle af \rangle \langle be \rangle \langle cd \rangle \\ &\equiv 4 \left(\delta_{\ell_1 \ell'_1}^{\mathcal{K}} W_{\ell_1}^L W_{\ell'_1}^{L'} C_{\ell_1}^g \times \delta_{\ell_2 \ell'}^{\mathcal{K}} W_{\ell_2}^L C_{\ell'}^g \times \delta_{\ell'_2 \ell}^{\mathcal{K}} W_{\ell'_2}^{L'} C_{\ell}^g \right) \end{aligned} \quad (C6)$$

where we have already noticed that both of these two terms will only contribute when filters are identical due to the products $\delta_{\ell_i \ell'_i}^{\mathcal{K}} W_{\ell_i}^L W_{\ell'_i}^{L'}$, which means all sub-contributions are equivalent ($a, b \leftrightarrow d, e$ is now valid since the FSBs must be the same).

Inserting these expressions back in the original formula for the FSB covariance, we find that the first group contributes in the diagonal only, while the second contributes within the filtered ranges along the main diagonal. These correspond respectively to D_{222} and N_{222} (already introduced in H25) in the 2-field case.

Their full expressions are:

$$\text{Cov}_{D_{222}} \left(\hat{\Phi}_{LL}^{ggk}, \hat{\Phi}_{L'L'}^{ggk} \right) = \frac{2C_{\ell}^{\mathcal{K}\mathcal{K}}}{(2\ell+1)} \delta_{\ell \ell'}^{\mathcal{K}} \sum_{\ell_{12}} \frac{(2\ell_1+1)(2\ell_2+1)}{4\pi} \begin{pmatrix} \ell & \ell_1 & \ell_2 \\ 0 & 0 & 0 \end{pmatrix}^2 W_{\ell_1}^{L, L'} W_{\ell_2}^{L, L'} C_{\ell_1}^{gg} C_{\ell_2}^{gg} \quad (C7)$$

$$\text{Cov}_{N_{222}} \left(\hat{\Phi}_{\ell}^{L(ggk)}, \hat{\Phi}_{\ell'}^{L'(ggk)} \right) = \frac{W_{\ell'}^L W_{\ell}^{L'} C_{\ell}^{gk} C_{\ell'}^{gk}}{\pi} \sum_{\ell_1} (2\ell_1+1) \begin{pmatrix} \ell & \ell_1 & \ell' \\ 0 & 0 & 0 \end{pmatrix}^2 W_{\ell_1}^L W_{\ell_1}^{L'} C_{\ell_1}^{gg} \quad (C8)$$

We have used the following property of the Gaunt coefficients to further simplify the two expressions:

$$\sum_{m_1 m_2 m_3} \left(\mathcal{G}_{m_1 m_2 m_3}^{\ell_1 \ell_2 \ell_3} \right)^2 = \frac{(2\ell_1+1)(2\ell_2+1)(2\ell_3+1)}{4\pi} \begin{pmatrix} \ell_1 & \ell_2 & \ell_3 \\ 0 & 0 & 0 \end{pmatrix}^2. \quad (C9)$$

There have been slight changes compared to the 1-field case: the spectra outside the sum are cross-spectra but the one inside is the auto spectrum of field g ; but it still retains its original behaviour – the term vanishes when the two filters are not identical.

Note that once again, we can write the N_{222} using the mode-coupling matrix \mathcal{M} (MCM; Eq. 14 in [Alonso et al. 2019](#)):

$$C8 = \frac{4W_{\ell'}^L W_{\ell}^{L'} C_{\ell}^{gk} C_{\ell'}^{gk}}{(2\ell'+1)} \sum_{\ell_1} \frac{(2\ell'+1)(2\ell_1+1)}{4\pi} \begin{pmatrix} \ell & \ell' & \ell_1 \\ 0 & 0 & 0 \end{pmatrix}^2 \left[W_{\ell_1}^L W_{\ell_1}^{L'} C_{\ell_1}^{gg} \right] = \frac{4W_{\ell'}^L W_{\ell}^{L'} C_{\ell}^{gk} C_{\ell'}^{gk}}{(2\ell'+1)} \mathcal{M} \left[W_{\ell_1}^L W_{\ell_1}^{L'} C_{\ell_1}^{gg} \right] \quad (C10)$$

C.1.2. $gg\kappa \times ggg$ covariance

It is rather straightforward to derive this cross-covariance, by simply swapping one κ field for a g field in the expressions derived in the previous section. This gives

$$\text{Cov}_{D_{222}} \left(\hat{\Phi}_{LL\ell}^{gg\kappa}, \hat{\Phi}_{L'L'\ell'}^{ggg} \right) = \frac{2C_\ell^{g\kappa}}{(2\ell+1)} \delta_{\ell\ell'}^{\mathcal{K}} \sum_{\ell_{12}} \frac{(2\ell_1+1)(2\ell_2+1)}{4\pi} \begin{pmatrix} \ell & \ell_1 & \ell_2 \\ 0 & 0 & 0 \end{pmatrix}^2 W_{\ell_1}^{L,L'} W_{\ell_2}^{L,L'} C_{\ell_1}^{gg} C_{\ell_2}^{gg}, \quad (\text{C11})$$

$$\text{Cov}_{N_{222}} \left(\hat{\Phi}_{LL\ell}^{gg\kappa}, \hat{\Phi}_{L'L'\ell'}^{ggg} \right) = \frac{W_{\ell'}^L W_{\ell}^{L'} C_{\ell}^{gg} C_{\ell'}^{g\kappa}}{\pi} \sum_{\ell_{1,2}} (2\ell_1+1) \begin{pmatrix} \ell & \ell_1 & \ell' \\ 0 & 0 & 0 \end{pmatrix}^2 W_{\ell_1}^L W_{\ell_1}^{L'} C_{\ell_1}^{gg}. \quad (\text{C12})$$

C.2. FSB-PCL covariances

C.2.1. $gg\kappa \times g\kappa$ covariance

The main term in the cross-covariance of an FSB and a power spectrum yields this time a 5 point correlation function:

$$\langle \hat{\Phi}_{LL\ell}^{gg\kappa} \hat{C}_{\ell'}^{g\kappa} \rangle = \frac{1}{(2\ell+1)(2\ell'+1)} \sum_{\ell_1\ell_2} W_{\ell_1}^L W_{\ell_2}^L \sum_{m,m',m_1,m_2} \mathcal{G}_{mm'm_1m_2}^{\ell\ell_1\ell_2} \langle g_{\ell_1 m_1} g_{\ell_2 m_2} \kappa_{\ell m} g_{\ell' m'} \kappa_{\ell' m'} \rangle \quad (\text{C13})$$

As before, we write

$$\langle g_{\ell_1 m_1} g_{\ell_2 m_2} \kappa_{\ell m} g_{\ell' m'} \kappa_{\ell' m'} \rangle \equiv \langle abcde \rangle$$

for simplicity, and now look at the “3 + 2” decomposition which gives rise to noticeable off-diagonal contributions in the 1-field case. This gives us the 10 following combinations:

$$\begin{aligned} \langle abcde \rangle_{32} &= \langle cde \rangle \langle ab \rangle + \langle bde \rangle \langle ac \rangle + \langle bce \rangle \langle ad \rangle + \langle bcd \rangle \langle ae \rangle \\ &+ \langle ade \rangle \langle bc \rangle + \langle ace \rangle \langle bd \rangle + \langle acd \rangle \langle be \rangle \\ &+ \langle abd \rangle \langle ce \rangle + \langle abe \rangle \langle cd \rangle \\ &+ \langle abc \rangle \langle de \rangle \end{aligned}$$

where we cancelled the terms that vanish due to the closed triangle condition. The last contribution cancels out with the counterterm $\langle X \rangle \langle Y \rangle$ of the covariance (Eq. C2), and as such we will ignore it for now. In the 1-field case, there were only 2 independent groups among the remaining 6 terms – the only discriminating factor was the number of filtered fields in each 2-point and 3-point functions respectively, but now one also needs to keep track of the number of κ fields in each.

This gives us 4 different groups; there are two diagonal terms (let’s label them D_{32}^a and D_{32}^b) and two off-diagonal terms (N_{32}^a and N_{32}^b). They are the following:

$$N_{32}^a = \langle bce \rangle \langle ad \rangle + \langle ace \rangle \langle bd \rangle = 2 \langle g_{\ell_2 m_2} \kappa_{\ell m} \kappa_{\ell' m'} \rangle \langle g_{\ell_1 m_1} g_{\ell' m'} \rangle = 2 W_{\ell'}^L W_{\ell_2}^L C_{\ell'}^g \delta_{\ell\ell'}^{\mathcal{K}} \mathcal{G}_{mm'm_2}^{\ell\ell_1\ell_2} b_{\ell\ell_1\ell_2}^{\kappa\kappa g} \quad (\text{C14})$$

$$D_{32}^a = \langle abd \rangle \langle ce \rangle \equiv \langle g_{\ell_1 m_1} g_{\ell_2 m_2} g_{\ell' m'} \rangle \langle \kappa_{\ell m} \kappa_{\ell' m'} \rangle = W_{\ell_1}^L W_{\ell_2}^L C_{\ell}^{\mathcal{K}} \delta_{\ell\ell'}^{\mathcal{K}} \mathcal{G}_{mm'm_2}^{\ell\ell_1\ell_2} b_{\ell\ell_1\ell_2}^{ggg} \quad (\text{C15})$$

$$D_{32}^b = \langle abe \rangle \langle cd \rangle + \langle abc \rangle \langle de \rangle \equiv 2 \langle g_{\ell_1 m_1} g_{\ell_2 m_2} \kappa_{\ell' m'} \rangle \langle \kappa_{\ell m} g_{\ell' m'} \rangle = 2 W_{\ell_1}^L W_{\ell_2}^L C_{\ell}^{g\kappa} \delta_{\ell\ell'}^{\mathcal{K}} \mathcal{G}_{mm'm_2}^{\ell\ell_1\ell_2} b_{\ell\ell_1\ell_2}^{\kappa gg} \quad (\text{C16})$$

$$N_{32}^b = \langle bcd \rangle \langle ae \rangle + \langle acd \rangle \langle be \rangle \equiv 2 \langle g_{\ell_2 m_2} \kappa_{\ell m} g_{\ell' m'} \rangle \langle g_{\ell_1 m_1} \kappa_{\ell' m'} \rangle = 2 W_{\ell'}^L W_{\ell_2}^L C_{\ell'}^{g\kappa} \delta_{\ell\ell'}^{\mathcal{K}} \mathcal{G}_{mm'm_2}^{\ell\ell_1\ell_2} b_{\ell\ell_1\ell_2}^{\kappa gg} \quad (\text{C17})$$

Inserting each into Eq. C13 gives

$$\text{Cov}_{D_{32}} \left(\hat{\Phi}_{LL\ell}^{gg\kappa}, \hat{C}_{\ell'}^{g\kappa} \right) = \text{Cov}_{D_{32}^a} \left(\hat{\Phi}_{LL\ell}^{gg\kappa}, \hat{C}_{\ell'}^{g\kappa} \right) + \text{Cov}_{D_{32}^b} \left(\hat{\Phi}_{LL\ell}^{gg\kappa}, \hat{C}_{\ell'}^{g\kappa} \right) = \frac{\delta_{\ell\ell'}^{\mathcal{K}}}{(2\ell+1)} \left(C_{\ell}^{\mathcal{K}} \Phi_{LL\ell}^{ggg} + C_{\ell}^{g\kappa} \Phi_{LL\ell}^{gg\kappa} \right) \quad (\text{C18})$$

$$\text{Cov}_{N_{32}} \left(\hat{\Phi}_{LL\ell}^{gg\kappa}, \hat{C}_{\ell'}^{g\kappa} \right) = \text{Cov}_{N_{32}^a} \left(\hat{\Phi}_{LL\ell}^{gg\kappa}, \hat{C}_{\ell'}^{g\kappa} \right) + \text{Cov}_{N_{32}^b} \left(\hat{\Phi}_{LL\ell}^{gg\kappa}, \hat{C}_{\ell'}^{g\kappa} \right) = \frac{2 W_{\ell'}^L}{(2\ell'+1)} \left(C_{\ell'}^{gg} \Phi_{L\ell'\ell}^{gg\kappa} + C_{\ell'}^{g\kappa} \Phi_{L\ell'\ell}^{gg\kappa} \right) \quad (\text{C19})$$

C.2.2. $gg\kappa \times gg$ and $ggg \times g\kappa$ covariances

Similarly to our approach for the $gg\kappa \times ggg$ covariance, we swap one κ field from the section above for a g field. The corresponding expressions now read

$$\text{Cov}_{D_{32}} \left(\hat{\Phi}_{LL\ell}^{gg\kappa}, \hat{C}_{\ell'}^{gg} \right) = \frac{2 \delta_{\ell\ell'}^{\mathcal{K}}}{(2\ell+1)} C_{\ell}^{g\kappa} \Phi_{LL\ell}^{ggg} \quad (\text{C20})$$

$$\text{Cov}_{N_{32}} \left(\hat{\Phi}_{LL\ell}^{gg\kappa}, \hat{C}_{\ell'}^{gg} \right) = \frac{4 W_{\ell'}^L}{(2\ell'+1)} C_{\ell'}^{gg} \Phi_{L\ell'\ell}^{gg\kappa} \quad (\text{C21})$$

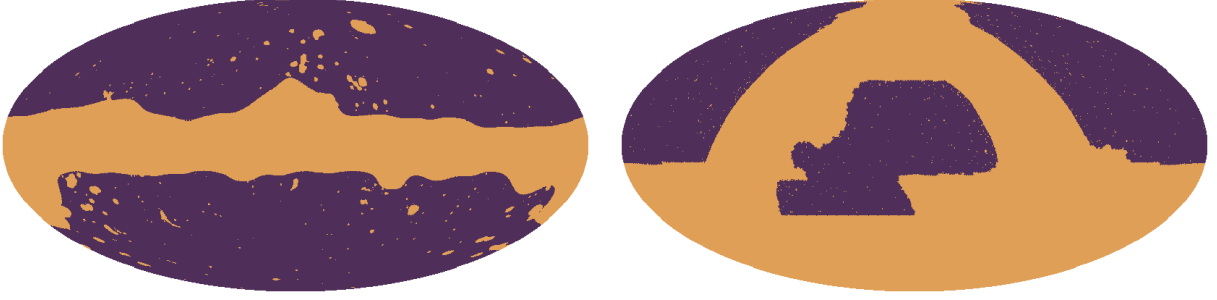


Figure 11. Binary masks used to check the accuracy of the f_{sky} scalings. The first mask (left) corresponds to the lensing convergence data used in this paper, while the second is typical of galaxy surveys like DESI. Note that we use both Galactic (left) and Equatorial (right). Their overlap thus leads to an f_{sky} value that is quite low compared to their individual f_{sky} values, making it easier to identify the correct f_{sky} scaling.

for the $g\kappa \times g\kappa$ covariance, and

$$\text{Cov}_{D_{32}} \left(\hat{\Phi}_\ell^{ggg} \hat{C}_{\ell'}^{g\kappa} \right) = \frac{\delta_{\ell\ell'}^{\mathcal{K}}}{(2\ell+1)} \left(C_\ell^{g\kappa} \Phi_{LL\ell}^{ggg} + C_\ell^{gg} \Phi_{LL\ell}^{g\kappa} \right) \quad (\text{C22})$$

$$\text{Cov}_{N_{32}} \left(\hat{\Phi}_{LL\ell}^{ggg} \hat{C}_{\ell'}^{g\kappa} \right) = \frac{2W_{\ell'}^L}{(2\ell'+1)} \left(C_{\ell'}^{gg} \Phi_{L\ell'\ell}^{gg\kappa} + C_{\ell'}^{g\kappa} \Phi_{L\ell'\ell}^{ggg} \right) \quad (\text{C23})$$

for the $ggg \times g\kappa$ case.

C.3. Calibrating the f_{sky} correction

As detailed in H25, we account for mode loss due to incomplete observations on the sky by dividing the off-diagonal contributions (N_{222} and N_{32}) by the effective sky fraction observed: since the sky fraction, defined as the mean of the square of the survey mask, is less than unity (signifying incomplete observations), the rescaling operation leads to an increase in the covariance. This empirical rescaling in the case of the FSB agrees well with the covariance obtained from simulations.

This poses no issues in the 1-field case, where the original field and its filtered-squared version share the same footprint on the sky; the choice of rescaling factor becomes less obvious when the two fields each have their respective masks. Take Eq. C8 for instance; the expression includes C_ℓ^{gg} and $C_\ell^{g\kappa}$, which were measured on different effective sky areas – in this case, should the N_{222} contribution be rescaled using $f_{\text{sky}} = \langle w_g w_g \rangle$ or $f_{\text{sky}} = \langle w_g w_\kappa \rangle$? The most conservative approach would be to always use the smallest effective sky fraction, as to not underestimate measurement errors, but this might be suboptimal.

Let us look at this problem from a theoretical perspective. Let us partition the mask associated with a field f into smaller, equal-area masks; those smaller masks make up a set which we label \mathcal{S} . For this we do not require the mask to be binary, as the following should also hold for non-binary masks as well. The power spectrum of f can be approximated on small scales by an average over the power spectra x_i of individual set elements $i \in \mathcal{S}$:

$$X = \frac{1}{N_{\mathcal{S}}} \sum_{i \in \mathcal{S}} x_i \quad (\text{C24})$$

where $N_{\mathcal{S}}$ is the number of elements in the set (which we can liken to $f_{\text{sky}} = N_{\mathcal{S}}/N_{\text{sphere}}$). The covariance of such an estimator X and another \tilde{X} defined on a different mask, assuming $\langle x_i \rangle = \langle \tilde{x}_i \rangle = 0$, is given by

$$\text{Cov}(X, \tilde{X}) = \frac{1}{N_{\mathcal{S}} N_{\tilde{\mathcal{S}}}} \sum_{i \in \mathcal{S}} \sum_{j \in \tilde{\mathcal{S}}} \langle x_i \tilde{x}_j \rangle. \quad (\text{C25})$$

As we do not expect different patches on the sky to be strongly correlated, we assume that $\langle x_i \tilde{x}_j \rangle$ only contributes when $i = j$ (a contribution which we label σ in that case). Of course, this approximation breaks in case the masks have no overlap. This allows us to further simplify the expression to

$$\text{Cov}(X, \tilde{X}) = \frac{1}{N_{\mathcal{S}} N_{\tilde{\mathcal{S}}}} \sum_{i \in \mathcal{S} \cap \tilde{\mathcal{S}}} \sigma = \frac{\sigma}{N_{\mathcal{S}} N_{\tilde{\mathcal{S}}}} N_{\mathcal{S} \cap \tilde{\mathcal{S}}}, \quad (\text{C26})$$

where $N_{\mathcal{S} \cap \tilde{\mathcal{S}}}$ is the number of patches belonging to both sets \mathcal{S} and $\tilde{\mathcal{S}}$. We can now interpret this result for our case study of the galaxy and convergence field:

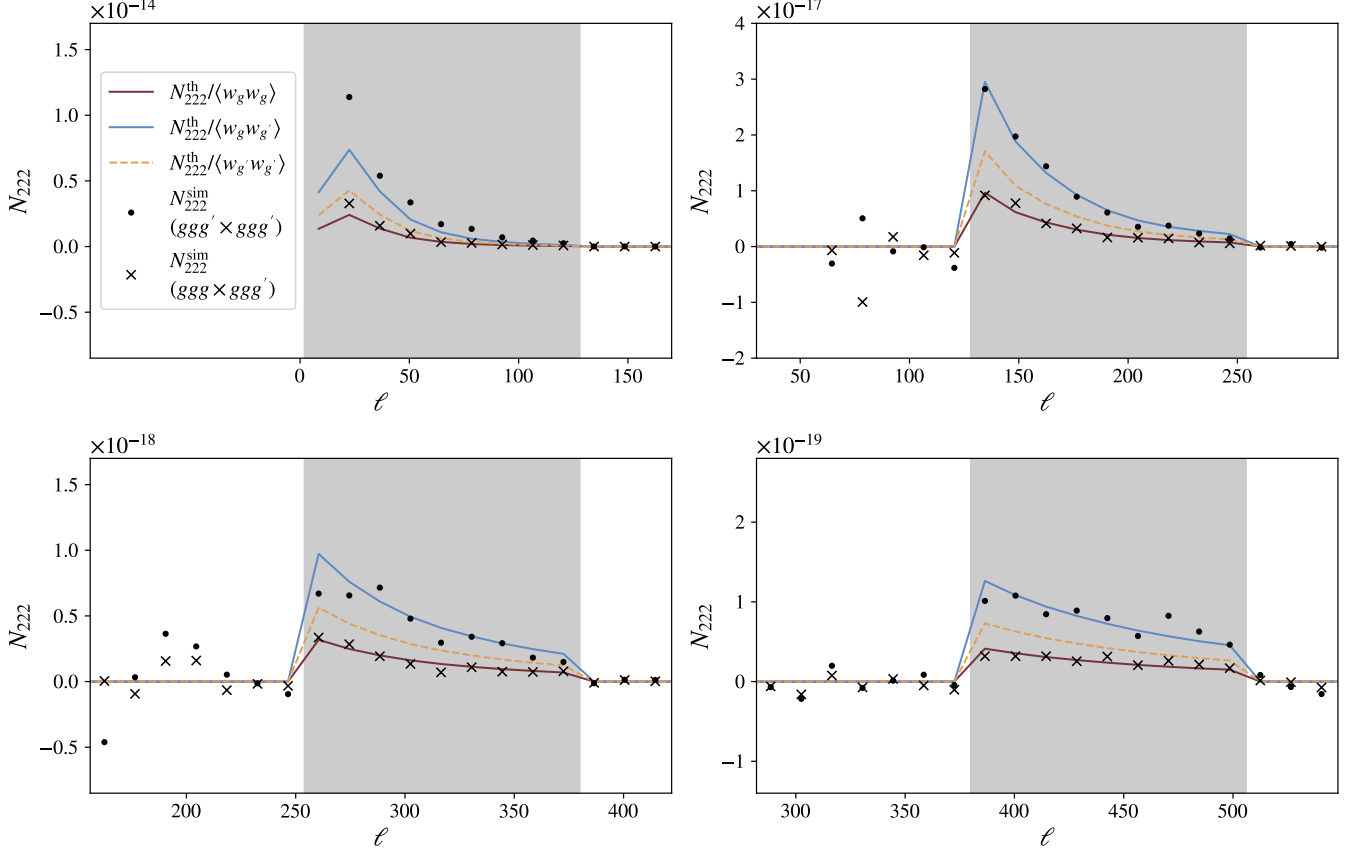


Figure 12. Scalings of Gaussian covariance term N_{222} with the effective sky fraction. The N_{222} term only contributes within the filtered range, which we have represented as the vertical grey band – each sub-figure therefore corresponds to a different FSB. The simulation-based $ggg \times ggg'$ cross-covariance (black dots) and $ggg' \times ggg'$ auto-covariance (black crosses) N_{222}^{sim} terms follow different scalings, as is shown by the coloured lines which represent the theoretical value of N_{222} in the full-sky scenario, scaled by different values of f_{sky} . The three values chosen here correspond to $\langle w_g w_g \rangle$ (solid brown line), $\langle w_g w_{g'} \rangle$ (solid blue line), and $\langle w_{g'} w_{g'} \rangle$ (dashed yellow line).

- For the covariance of $\hat{\Phi}_{LL\ell}^{gg\kappa}$ and $\hat{\Phi}_{L'L'\ell'}^{gg\kappa}$, both quantities are defined over the same effective sky fraction, given by the intersection of the g and κ masks. In this case, N_S , $N_{\bar{S}}$ and $N_{S \cap \bar{S}}$ are all identical, and consequently the covariance should be scaled by $f_{\text{sky}} = \langle w_g w_\kappa \rangle$.
- For the covariance of $\hat{\Phi}_{LL\ell}^{gg\kappa}$ and $\hat{\Phi}_{L'L'\ell'}^{ggg}$, $N_{\bar{S}}$ is a subset of N_S by definition, since one power spectrum (ggg FSB) is defined over the g mask, while the other ($gg\kappa$) has for effective sky fraction the intersection of the g and κ masks. $N_{\bar{S}}$ and $N_{S \cap \bar{S}}$ are therefore the same and cancel out, such that the expression must scale with $f_{\text{sky}} = \langle w_g w_g \rangle$.

We check these results by calibrating this rescaling factor using Gaussian simulations: N_{222} being a fully disconnected term, it should appear in the covariance even if the fields are fully Gaussian. Comparing the possible rescalings of the analytical N_{222} with the covariance obtained from measuring FSBs on Gaussian fields with different masks, should give us an idea of which f_{sky} correction is most accurate. To measure N_{222} on simulations, one must make sure that fields g and κ are correlated, as N_{222} depends on the cross-power spectrum of the two fields. To enhance the N_{222} signal, we instead use the same field for both g and κ , but use different masks for each – we shall now call both fields g and g' , and their respective masks w_g and $w_{g'}$. We chose the masks so that possible combinations of effective sky fractions lead to values that are distinguishable from one another. The two masks, shown in Fig. 11, have little overlap, and give the following f_{sky} values: $\langle w_g w_g \rangle = 0.68$, $\langle w_g w_{g'} \rangle = 0.38$, $\langle w_{g'} w_{g'} \rangle = 0.22$.

We computed N_{222} in the case of the auto-covariance $\text{Cov}(\Phi_{LL\ell}^{ggg'}, \Phi_{L'L'\ell'}^{ggg'})$ from Eq. C8 and the cross-covariance $\text{Cov}(\Phi_{LL\ell}^{ggg}, \Phi_{L'L'\ell'}^{ggg'})$ from Eq. C12 over a total of 2400 Gaussian simulations. The simulation-based, isolated N_{222} terms were computed as the difference between the simulation-based covariance and the Gaussian covariance computed from assuming g_L^2 and g are Gaussian fields (see Section 2.1.3). Taking this difference should successfully isolate N_{222} , as the subdominant connected terms we do not account for in our covariance model vanish for Gaussian fields.

The N_{222} expressions for $\text{Cov}(\Phi_{LL\ell}^{ggg'}, \Phi_{L'L'\ell'}^{ggg'})$ and $\text{Cov}(\Phi_{LL\ell}^{ggg}, \Phi_{L'L'\ell'}^{ggg'})$ depend on auto- and cross-power spectra of g and g' , but Fig. 12 shows that they have different f_{sky} scalings, which seem to agree with our theoretical expectations: the $ggg' \times ggg'$ term does indeed scale with $\langle w_g w_{g'} \rangle$ (the black dots on Fig. 12 closely follow the blue line across all FSBs), and the $ggg' \times ggg'$ term with $\langle w_g w_g \rangle$ (the black crosses match the brown line).

Our measurements of N_{222} are therefore easily explained by our simple theoretical considerations (Eq. C26), and can be generalised to the connected N_{32} terms. We repeat below all relevant scalings for completeness:

$$\text{Cov}\left(C_{\ell}^{gg}, C_{\ell'}^{gg}\right) \sim \text{Cov}\left(\Phi_{LL\ell}^{ggg}, C_{\ell'}^{gg}\right) \sim \text{Cov}\left(\Phi_{LL\ell}^{ggg}, \Phi_{\ell'}^{ggg}\right) \propto \langle w_g w_g \rangle^{-1}, \quad (\text{C27})$$

$$\text{Cov}\left(C_{\ell}^{gk}, C_{\ell'}^{gg}\right) \sim \text{Cov}\left(\Phi_{LL\ell}^{ggk}, C_{\ell'}^{gg}\right) \sim \text{Cov}\left(\Phi_{LL\ell}^{ggg}, C_{\ell'}^{gk}\right) \sim \text{Cov}\left(\Phi_{LL\ell}^{ggk}, \Phi_{L'L'\ell'}^{ggg}\right) \propto \langle w_g w_g \rangle^{-1}, \quad (\text{C28})$$

$$\text{Cov}\left(C_{\ell}^{gk}, C_{\ell'}^{gk}\right) \sim \text{Cov}\left(\Phi_{LL\ell}^{ggk}, C_{\ell'}^{gk}\right) \sim \text{Cov}\left(\Phi_{LL\ell}^{ggk}, \Phi_{L'L'\ell'}^{ggk}\right) \propto \langle w_g w_k \rangle^{-1}. \quad (\text{C29})$$

D. INTERPOLATOR PERFORMANCE

We test the performance of the interpolator used in this paper, both in terms of accuracy and runtime. There are technically two stages in the bispectrum interpolator where we make use of interpolation:

- (i) First, instead of computing the bispectrum at each (ℓ_1, ℓ_2, ℓ_3) , we define a subset of multipoles, then interpolate linearly in 3D to evaluate missing configurations. The multipole subset we use here contains all multipoles between 0 and 10, then every 20 multipole from 10 to 96, and 50 multipoles logarithmically spaced between 100 and ℓ_{max} .
- (ii) We then build a cubic Ω_m -interpolator, as the bispectrum Ω_m dependence is more complex and cannot be accounted for by a simple linear rescaling of the templates. We compute the FSB templates for 100 values of Ω_m linearly spaced in the range $0.05 \leq \Omega_m < 0.5$; for a given value of Ω_m , we can then interpolate the FSB from neighbouring values of Ω_m .

The final interpolator is then a result of these two interpolations, at the level of the projected bispectrum templates (multipole interpolation), and at the FSB templates level (Ω_m interpolation).

We start by verifying that the overall accuracy of the interpolator is acceptable: we show in Fig. 13 that the interpolator works exquisitely well for the power spectra, and is slightly biased in the case of the bispectrum. Indeed, we report a difference between interpolation and full calculation of the FSB corresponding to $\sim 5\%$ of the errors on the ggg measurement, which we deem acceptable. We investigate the source of this bias by computing the difference between the two approaches for each template contributing to the deterministic part of the ggg FSB (see definitions in Eq. 25); we show this in the left panel of Fig. 14. The largest error on individual projected templates (at fixed Ω_m and σ_8 , and before accounting for the bias rescaling) is found for the T_2 template with a bias of about $\lesssim 15\%$ of the full-calculation template. However, it is not the main contribution to the overall error budget, as the linear contribution F_2 accounts for most of the bispectrum signal. In blue, we also show the much smaller errors that could be achieved using a cubic interpolator at the multipole level (instead of a linear one, shown in red). In this case, the interpolation bias is barely noticeable, but the making of such cubic interpolators is very costly in 3D, even at small ℓ_{max} . To generate 100 FSB templates (i.e. 5 templates for each Ω_m value to build the interpolator), and allocating the same computational resources in both cases, the linear approach to interpolation takes about 4 minutes, but the cubic approach is closer to 38 hours. This could easily be sped up using parallelisation, and once built, the interpolator is fast to evaluate – whether it is linear or cubic; however, given our error budget and various approximations taken in this work, it is not yet necessary to refine the bispectrum interpolator to achieve sub-percent accuracy.

In the right panel of Fig. 14, we also show the time gain that can be obtained from using the interpolator. This gain evidently depends on the number of triangle contributions that need to be computed, which increases with the maximum multipole used in the analysis, ℓ_{max} . Since we selected a large-scale filter for the inference part of this work, the signal of the FSB dies off at reasonably low ℓ , but the time gain is already consequential: to estimate a single F_2 template, for identical binning and cosmological parameters, the interpolator is 9 times faster to evaluate than the full bispectrum. However, we could have selected larger filters in the highest redshift bins – Fig. 4 makes this obvious – which would have then made us compute the bispectrum up to $\ell_{\text{max}} \sim 300$. Reading from the plot, this corresponds to a $\sim \times 30$ improvement in runtime when using the interpolator over the full calculation¹⁰. We do not show the same plot for Q_2 and T_2 , since F_2 can partly be derived from these two templates – once you compute F_2 , you effectively get Q_2 and T_2 for free if you save the various terms of F_2 separately (see Eq. 25). A full MCMC chain for the ggg data vector with 50,000 samples takes 0.6 hours to run on 8 cores, therefore we can expect a chain to take more than 5 hours to complete on the same number of cores using the full bispectrum calculation – which is not unfeasible given appropriate computing resources, but might become so if we push the calculation to smaller scales.

This paper was built using the Open Journal of Astrophysics L^AT_EX template. The OJA is a journal which provides fast and easy peer review for new papers in the astro-ph section of the arXiv, making the reviewing process simpler for authors and referees alike. Learn more at <http://astro.theoj.org>.

¹⁰ We do not claim however that our implementation of the tree-level

bispectrum calculation is fully optimized.

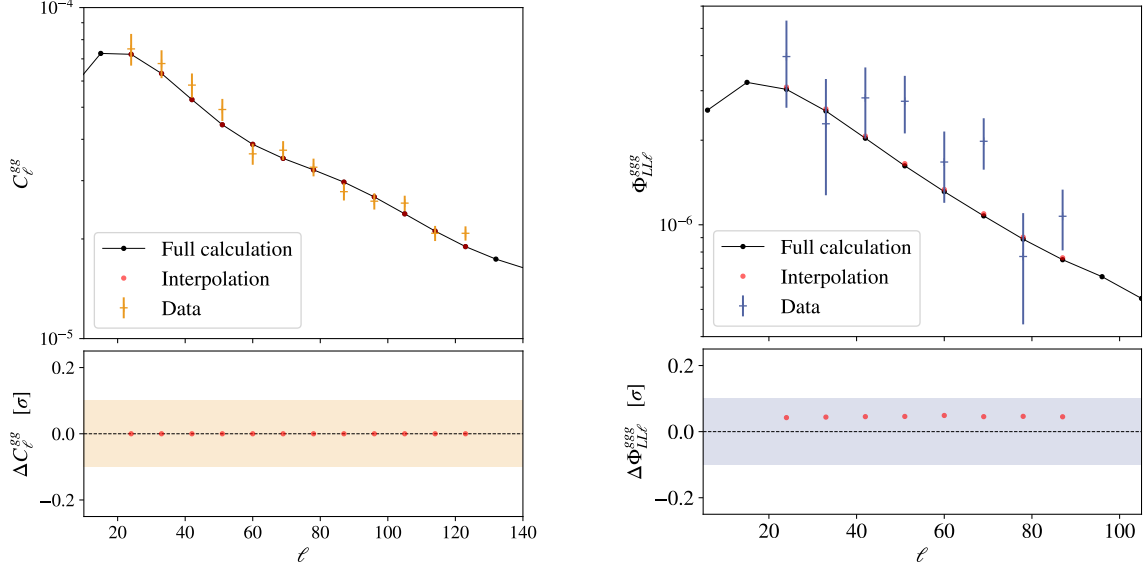


Figure 13. Interpolator accuracy. *Left panel:* We compare the power spectrum best-fit obtained from the interpolation (which comprises an interpolation at the multipole level, and an interpolation between values of Ω_m) and the full calculation of the power spectrum. The difference between the two approaches is less than 0.003% of the error σ associated with the measurement. *Right panel:* We show the same comparison for the ggg FSB best-fit. The difference between the interpolation and full calculation corresponds in that case to about 5% of the error associated with the measurement. In both lower panels, we show in colour the interval corresponding to 10% of the error bars in the upper panels.

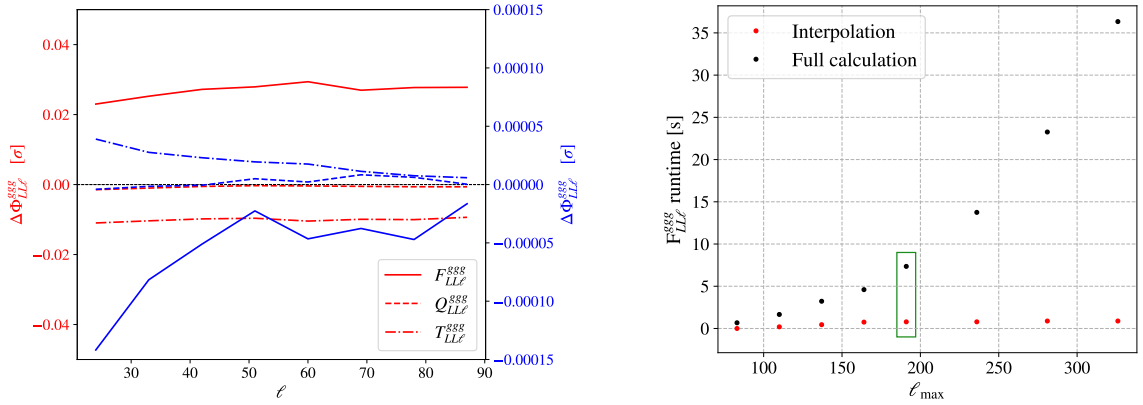


Figure 14. Details by templates. *Left panel:* Interpolated best-fit template errors with respect to the full calculation, for the individual templates of the ggg FSB. We do not show the interpolated noise templates, which depend on power spectra (which are themselves recovered to high precision by the interpolator, as shown in the left panel of Fig. 13). The red lines were obtained using linear interpolation between multipoles, while the blue lines show the equivalent for a cubic interpolator. Note how the right axis (cubic interpolation) is about 300 times smaller than the left axis (linear interpolation). *Right panel:* Runtime performance of the interpolator (red dots) compared to computing the full calculation (black dots) for one F_{LL}^{ggg} template, as a function of maximum scale ℓ_{\max} . As we increase ℓ_{\max} , the number of triangle configurations contributing to the bispectrum dramatically increases, making the full calculation unsuitable for inference purposes. We highlight the data points relevant to this paper in a green box: for a scale cut of $\ell_{\max} = 191$, interpolating is more than 9 times faster than computing the full bispectrum.